JGR Oceans

RESEARCH ARTICLE
10.1029/2021JC018261

On Internal Tides Driving Residual Currents and Upwelling on an Island

Justin S. Rogers[1], Frederick T. Mayer[1], Kristen A. Davis[2], and Oliver B. Fringer[1]

[1]Bob and Norma Street Environmental Fluid Mechanics Laboratory, Stanford University, Stanford, CA, USA, [2]Department of Civil and Environmental Engineering and Earth System Science, University of California, Irvine, CA, USA

Key Points:

- Internal tides interacting with an island force complex residual currents and upwelling
- Rotation, barotropic tides, large-scale mean currents and bottom slope all have an influence on the currents and upwelling
- Subcritical slope has the largest upwelling from internal tides and the greatest potential for creating thermal refugia in a warming ocean

Supporting Information:

Supporting Information may be found in the online version of this article.

Correspondence to:

J. S. Rogers,
jsrogers@stanford.edu

Citation:

Rogers, J. S., Mayer, F. T., Davis, K. A., & Fringer, O. B. (2022). On internal tides driving residual currents and upwelling on an island. *Journal of Geophysical Research: Oceans*, *127*, e2021JC018261. https://doi.org/10.1029/2021JC018261

Received 19 NOV 2021
Accepted 13 JUN 2022

Author Contributions:

Conceptualization: Justin S. Rogers, Frederick T. Mayer, Kristen A. Davis, Oliver B. Fringer
Formal analysis: Justin S. Rogers
Investigation: Justin S. Rogers
Methodology: Justin S. Rogers
Software: Justin S. Rogers, Oliver B. Fringer
Validation: Justin S. Rogers
Visualization: Justin S. Rogers
Writing – original draft: Justin S. Rogers
Writing – review & editing: Justin S. Rogers, Frederick T. Mayer, Kristen A. Davis, Oliver B. Fringer

Abstract We present a modeling study of an idealized island with sloping sides in a stratified ocean with internal tides propagating through the domain, which transform into nonlinear internal waves as they encounter shallow depths. In the base condition, representative of a mid-latitude island with relatively steep super critical slopes, the nonlinear internal waves shoaling on the island wrap around the island, scatter, and create an asymmetric wavefield. Radiation stress gradients from this wavefield and rotation are balanced by pressure gradients and turbulent vertical diffusion in the momentum equations which drive residual mean currents around the island. We explore the effects of different physical parameters including no rotation, higher Froude number, subcritical slope, addition of barotropic tides, larger excursion number, and addition of large-scale mean currents. All simulations showed formation of residual currents of varying intensity, upwelled deep waters in shallow regions, and cooler waters on the side of the island consistent with the direction of incoming internal tides. While the no rotation and strong mean flow conditions created some upwelling, of all the modeled conditions, the subcritical slope has the greatest potential for creating favorable conditions for benthic organisms through enhanced upwelling. Areas of the world's oceans with stratified waters sufficient to sustain internal tide motions, strong internal tide energy, and local subcritical bottom slopes are likely to have cooler waters and more upwelled deep waters than the surrounding areas, and potentially serve as thermal refugia from future ocean warming.

Plain Language Summary Tides oscillate the world's oceans, and because warmer lighter water sits on cooler dense water, wave energy travels along this interface. This process, called internal tides, creates waves which propagate in the ocean interior and are quite common in the ocean. When these waves encounter a coastline or island they function similarly to waves on a beach: they can turn, change shape, break, or reflect. These changes to the waves can create currents, often quite strong, and pull deeper cooler water into the shallow coastal areas. We performed a modeling study to determine which factors are most important in creating strong currents from these internal tides across a range of possible conditions on islands worldwide. The results show that the internal tides create complex currents and bring cooler dense water into the shallow regions under most conditions. The factor that creates potentially the best conditions for organisms living on the ocean floor is gradual ocean floor slopes (compared to steeper). The results for this condition had strong currents, increased deep ocean waters, and cooler temperatures in the shallow coastal areas which may buffer effects from future ocean warming.

1. Introduction

Internal tides play a crucial role in the ocean's global redistribution of heat and momentum (Alford et al., 2015) and serve important ecological functions to mixing in the nearshore environment (Davis et al., 2020; Suanda et al., 2017; Walter et al., 2012). Upon encountering topography, internal tides propagate shoreward and evolve into nonlinear internal waves, with the leading edge often steepening into a bore front (Chao et al., 2006; McSweeney et al., 2019; Scotti et al., 2007). Upon further propagation into shallow depths, internal waves steepen and break, often forming dissipative bores (Arthur & Fringer, 2016; Walter et al., 2012). Internal tides propagating along ocean boundaries can form complex residual currents (Winters, 2015). In addition, forcing from tidal motions can lead to resonance of trapped internal Kelvin waves leading to large-amplitude internal tides in shallow coastal waters (Masunaga et al., 2017). These features lead to a complicated internal wavefield comprising waves of many frequencies and wave lengths, propagating in many directions from multiple sources, some for a great distance (Lamb, 2014; Nash et al., 2004). Of the energy lost from the barotropic tide, a study of Monterey Bay California showed approximately 88% is converted into baroclinic energy through internal tide generation, and

42% of this baroclinic energy radiates away into the open ocean, but this tidal energy partitioning depends greatly on the topographic features (Kang & Fringer, 2012).

For bores that approach shallow shores, three potential bore fates have been observed: (a) bores transiting intact to very shallow depths less than 10 m, (b) bores being overrun by faster, subsequent bores, leading to bore-merging events, and (c) bores dissipating when the upstream pycnocline is near or below mid-depth (McSweeney et al., 2019). Additionally, internal tides on relatively steep island slopes have been observed to partially reflect off the slope and transport dense cooler fluid shoreward within trapped cores (Davis et al., 2020).

Internal gravity waves can generate residual currents by dissipating energy through breaking and other processes, or by changes to wave direction such as reflection, diffraction and refraction. The spatial change in wave energy creates a net radiation stress or momentum flux in shallow waters proportional to the flux of energy lost from the waves. The basic mechanisms for generating residual mean flows is often evaluated with the Navier-Stokes momentum equations whereby the radiation stress gradient is balanced by a frictional boundary stress so that a time-averaged current is generated (Hogg, 1971; Thorpe, 1999). In addition, other forcing mechanisms can influence this momentum balance, of which rotation is especially important. Rotation affects both the internal wave properties (steepening, propagation speed, etc.) (Helfrich, 2007), as well the mean currents.

Shoaling internal waves have been observed to transport cooler nutrient-rich waters onto shallow depths in a variety of settings on continental shelves and islands (Davis et al., 2020; Lamb, 2014; Reid et al., 2019; Walter et al., 2012). Shoaling internal waves can thus reduce the overall thermal stress on reefs and potentially provide thermal refuges from ocean warming (Storlazzi et al., 2020; Wyatt et al., 2020). In addition, water motions from internal waves and mean currents can upwell nutrients and create enhanced phytoplankton biomass which drive marine ecosystems on islands (Gove et al., 2016; Wang et al., 2007). Thus, while it is well known that internal tides can create upwelled nutrient-rich, cooler waters, favorable for ecosystems, the exact mechanisms for formation of these residual currents and upwelling, and the relative importance of drivers have not been systematically explored.

To address this gap, this work examines in detail the mechanisms for internal tide generation of residual currents and upwelled waters on islands under a range of conditions. We first examine internal tide theory, setup a framework for exploring drivers of the system (Section 2.1), and describe the hydrodynamic model setup of an idealized island and equations for analysis using the SUNTANS model (O. B. Fringer et al., 2006) (Section 2.2). We then describe the mechanisms for internal tide shoaling and transformation (Section 3.1), the mechanism driving residual currents (Section 3.2), upwelling effects (Section 3.3), and ecologically relevant effects (Section 3.4). We follow with a summary (Section 4).

2. Theory and Model Setup

The setting we wish to investigate is internal tides propagating through the ocean interior, steepening into nonlinear internal waves, and interacting with an island to produce residual mean currents and upwelling. While islands can be complex in terms of their geometric properties and acted upon by complex time- and spatial scale of water movements, here we simplify the problem by isolating only the essential elements. We begin with an idealization of Dongsha Atoll in the South China Sea which is subject to strong internal tides and has been well studied (Davis et al., 2020; Lien et al., 2014; Ramp et al., 2010) (Figure 1). The idealized circular island of width W, sloping sides with slope S, rising to the ocean surface and surrounded by a domain of constant depth H in a stratified fluid with background density $\rho_b(z)$ (Figure 1, Table 1), is not unlike many islands worldwide and thus a useful framework for characterizing general behavior.

2.1. Formulation and Dimensional Analysis

In the presence of rotation f, internal waves with period t_0 and frequency $\omega_0 = 2\pi/t_0$ can exist with wavenumber $\boldsymbol{k} = \boldsymbol{k}(k, l, m)$ corresponding to x, y, z directions when their frequency satisfies $N^2 > \omega_0^2 > f^2$, and $_0$ represents the offshore location. Here, buoyancy frequency N given by $N^2 = \frac{g}{\rho_0}\frac{d\rho_b}{dz}$, which provides the restoring force, ρ_0 is the constant reference density, $\rho_b(z)$ is the background density, and g is gravitational acceleration. These waves

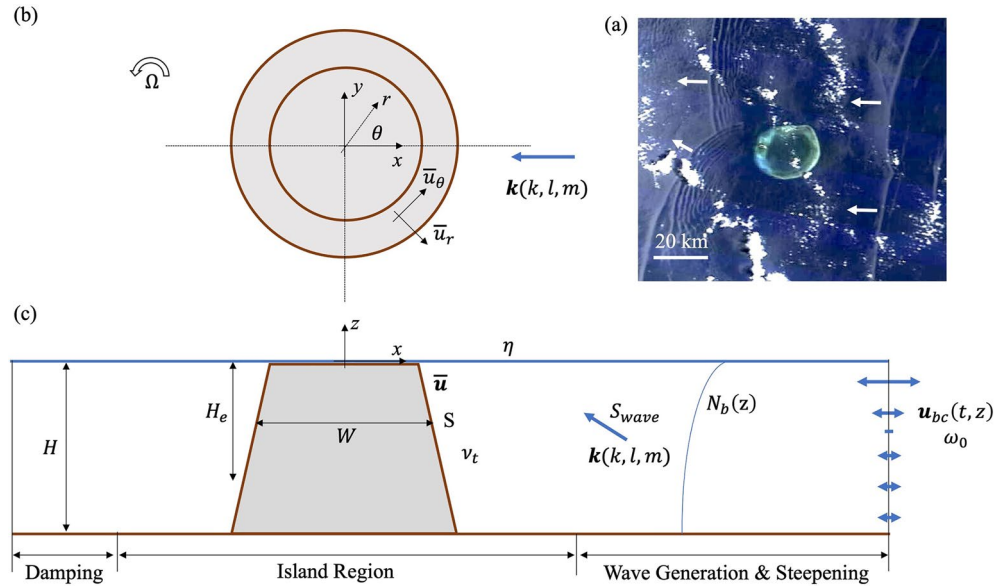

Figure 1. Island domain layout showing (a) representative image of Donghsa Atoll with shoaling internal tides traveling from right to left, and idealized island domain layout view from (b) top and (c) side showing internal tide forcing residual mean flows in the along-slope $\overline{u}_\theta$ and cross-slope $\overline{u}_r$ directions in a rotating frame Ω. Internal tides are forced at the boundary with velocity u_{bc} at frequency ω_0 and propagate through a stratified fluid of depth H with buoyancy frequency N_b and effective depth H_e at an angle S_{wave} producing movements in the free surface η steepening to nonlinear internal waves. The waves interact with a circular island of width W with sloping sides of slope S producing an eddy diffusivity ν_t. (a) taken from Terra/MODIS imagery from 26 May 2021 (https://worldview.earthdata.nasa.gov).

propagate in three dimensions but with a slope relative to the horizontal of $S_w = \frac{l}{k} = \left[\frac{\omega^2 - f^2}{N^2 - \omega^2}\right]^{\frac{1}{2}}$ (Hall et al., 2013; Wunsch, 1968). The waves also have a characteristic horizontal celerity given by $C = C_0\left[1 - \left(\frac{f}{\omega}\right)^2\right]^{\frac{1}{2}}$, where the speed in the absence of rotation is $C_0 = \frac{\omega}{k} \cong \frac{H_e}{\pi}\left(N_{\max}^2 - \omega^2\right)^{\frac{1}{2}}$ (Helfrich, 2007), where k is pointed in the same direction as wave propagation, and $N_{\max}$ is the maximum N at the pycnocline. H_e is the effective internal interface depth of the pycnocline (i.e., an approximation of the upper layer depth in a two-layer system) which depends on the normal modes solution for a continuous stratification (see Text S2 in Supporting Information S1, and Figure 2e) (S. Vitousek & Fringer, 2014). In addition, barotropic waves travel at the long-wave speed $C_{BT} = \sqrt{gH}$, where H is the total depth. Although C_0 is dependent on ω_0 in the presence of rotation, we assume the dependence is generally weak, and specifically, there is no nonhydrostatic frequency dispersion because the waves are generally hydrostatic. Note that the preceding formulations are primarily for linear internal tides, which is reasonable for understanding offshore behavior in deep waters away from shallow topographic features (where waves may become highly nonlinear).

In a general velocity field, we can isolate the internal wave motions by decomposing the Eulerian velocity $\boldsymbol{u}(u, v, w)$ into

$$\boldsymbol{u} = \overline{\boldsymbol{u}} + \tilde{\boldsymbol{u}} = \left(\overline{\boldsymbol{U}} + \overline{\boldsymbol{u}}'\right) + \left(\tilde{\boldsymbol{U}} + \tilde{\boldsymbol{u}}'\right) \tag{1}$$

which on the RHS are the low-frequency barotropic and baroclinic and the high-frequency barotropic and baroclinic (wave) terms, respectively. Here, we adopt a decomposition of variables into time high-pass ($\tilde{}$) and time low-pass ($\bar{}$) components with filtering time scale of two wave periods, $\tau_{\text{filt}} = 2t_0$, where the barotropic velocity is given by the depth average $\boldsymbol{U} = \frac{1}{H}\int_{-d}^{\eta} \boldsymbol{u}_H \, dz$ and $(\boldsymbol{\prime})$ denotes the deviation from the barotropic velocity (i.e., $\boldsymbol{u} = \boldsymbol{U} + \boldsymbol{u}'$).

Thus, we have the following set of independent variables in the idealized problem (Figure 1),

Table 1
Simulation Details

	R1. Base case	R2. No rotation	R3. Higher Fr	R4. Lower S	R5. Higher $\tilde{\boldsymbol{U}}_0$	R6. Higher ex	R7. Higher $\overline{\boldsymbol{U}}_0$
Variable modified from R1	-	Lower f	Lower N	Lower S	Higher $\tilde{U}_0$	Lower W	Higher $\overline{U}_0$
$\tilde{u}_0$ (m/s)	0.15	0.15	0.15	0.15	0.15	0.15	0.15
C_0 (m/s)	1.55	1.55	1.10	1.55	1.55	1.55	1.55
N_{max} (cps)	0.016	0.016	0.011	0.016	0.016	0.016	0.016
f (rad s^{-1})	5.70E−05	0	5.70E−05	5.70E−05	5.70E−05	5.70E−05	5.70E−05
S	0.0500	0.0500	0.0663	0.0075	0.0500	0.0450	0.0500
S_{wave}(max)	0.0083	0.0090	0.0117	0.0083	0.0083	0.0083	0.0083
$\tilde{U}_0$ (m/s)	0	0	0	0	0.15	0	0
$\overline{U}_0$ (m/s)	0	0	0	0	0	0	−0.05
$W(H_e/2)$ (m)	2.60E+04	2.60E+04	2.60E+04	4.50E+04	2.60E+04	1.10E+04	2.60E+04
Ro, $\frac{\omega_0}{f}$	2.465	Inf	2.465	2.465	2.465	2.465	2.465
Fr, $\frac{\tilde{u}_0}{C_0}$	0.097	0.097	0.137	0.097	0.097	0.097	0.097
$\alpha = \frac{S}{S_{\text{wave}}}$	6.050	5.530	5.672	0.907	6.050	5.445	6.050
BT tide, $\frac{\tilde{U}_0}{\tilde{u}_0}$	0.00	0.00	0.00	0.00	1.00	0.00	0.00
Ex, $\frac{\tilde{u}_0}{\omega_0 W}$	0.041	0.041	0.041	0.024	0.041	0.097	0.041
BT mean, $\frac{\overline{U}_0}{\tilde{u}_0}$	0	0	0	0	0	0	0.333
$FrEx^{-1} = \frac{\omega_0}{\omega_k}$	2.359	2.359	3.336	4.083	2.359	0.995	2.359
Bu, $\frac{L_R}{W}$	1.045	Inf	0.739	0.604	1.045	2.477	1.045

Note. Runs R1, R2, R4, R5, R6, and R7 were with representative summer stratification, while R3 was with representative winter stratification and reduced N. The following parameters were the same for all simulations: $\omega_0 = 1.41 \times 10^{-4}$ 1/s, $t_0 = t_{M2} = 12.42$ hr, $\overline{\tilde{u}}_0 = 0$, $g = 9.81$ m/s^2, $\nu_t = 1 \times 10^{-3}$ m^2/s, $\nu_{tH} = 1 \times 10^{-1}$ m^2/s, $H = 600$ m, $H_e = 313$ m, $C_D = 0.0025$, $C_{BT} = 76.7$ m/s, Re $= 1.61 \times 10^5$, $T_0 = 27.94$°C.

$$\left(\overline{\boldsymbol{u}}, \tilde{u}_0, \overline{\boldsymbol{U}}_0, \tilde{\boldsymbol{U}}_0, \omega_0, C_0, C_{BT}, f, S, W, \nu_t\right) \tag{2}$$

The applied boundary velocity $\tilde{u}_0$ is the scale of the offshore oscillatory wave motion, $\overline{\boldsymbol{U}}_0$ is the offshore barotropic mean flow, $\tilde{\boldsymbol{U}}_0$ is the scale of the offshore barotropic tidal flow, and $\overline{\boldsymbol{u}}$ is the resulting residual mean flow of interest near the island. Because this is a wave-dominated problem, we use ω_0^{-1} as the characteristic timescale, and the wave-excursion distance for the characteristic length scale, consistent with (Thorpe, 1999),

$$\text{Time} = \omega_0^{-1}$$

$$\text{Horizontal Length} = \tilde{u}_0 \omega_0^{-1}$$

$$\text{Vertical Length} = H_e$$

which after applying the Buckingham Pi theorem gives

$$\frac{\overline{\boldsymbol{u}}}{\tilde{u}_0} = \frac{\overline{\boldsymbol{u}}}{\tilde{u}_0}\left(\frac{\omega_0}{f}, \frac{\tilde{u}_0}{C_0}, S, \frac{\tilde{\boldsymbol{U}}_0}{\tilde{u}_0}, \frac{\tilde{u}_0}{\omega_0 W}, \frac{\overline{\boldsymbol{U}}_0}{\tilde{u}_0}, \frac{\tilde{u}_0}{C_{BT}}, \frac{\tilde{u}_0^2}{\omega_0 \nu_t}\right) \tag{3}$$

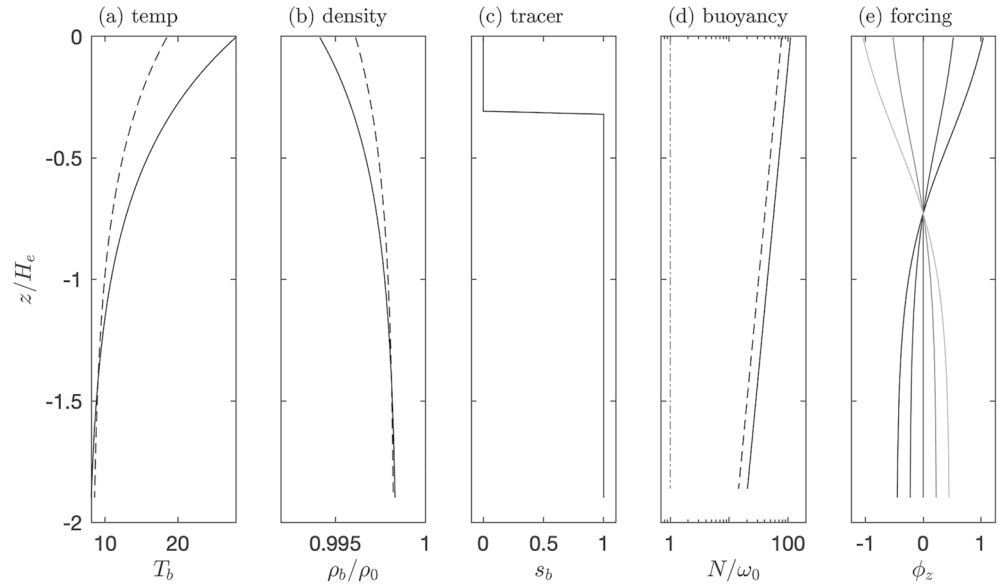

Figure 2. Profile of initial conditions and forcing function showing (a) background temperature T_b (b) normalized background density ρ_b/ρ_0, (c) passive background tracer s_b, (d) normalized buoyancy frequency N/ω_0 with lower limit for wave propagation $N/\omega_0 = 1$ (-.), and (e) wave forcing eigenfunction ϕ_z showing range of oscillations in time. In (a, b, and d), R1 (Base Case) summer stratification (-) and R3 winter stratification (--).

This result provides significant intuition on the interaction of the waves with the island to produce the resulting residual current $\frac{\overline{u}}{\tilde{u}_0}$. From left to right these terms are,

1. *Temporal Rossby number* (inertia-Coriolis), $Ro = \frac{\omega_0}{f} = \frac{2\pi C_0}{f\lambda_0}$, with respect to the wave traveling with wavelength λ_0 and speed C_0. A large Ro implies no rotational effect on the wave, while a small Ro approaching one implies a large rotational effect where wave motions feed energy to the inertial motions. For $Ro < 1$ all wave motions become inertial and propagating internal waves cannot exist.
2. *Froude number* (nonlinearity), $Fr = \frac{\tilde{u}_0}{C_0} = \frac{t_0\tilde{u}_0}{\lambda_0}$. A large Fr approaching one implies nonlinear waves, while a small *Fr* implies linear waves. Additionally, if $N \gg \omega$, $C_0 = H_e N/\pi$, and this term can be written as $\pi\frac{\tilde{u}_0}{H_e N}$.
3. *Bottom slope S.* Dividing the topographic slope by the wave slope S_w gives $\alpha = \frac{S}{S_w}$, which is a measure of the critical slope. When $\alpha > 1$ the internal wave is supercritical and reflections are important, and when $\alpha < 1$ the internal wave is subcritical and most wave energy propagates onshore and dissipates. For variable slopes and stratification, the fraction of energy reflected is primarily dependent on the maximum slope criticality (Hall et al., 2013).
4. *Barotropic tide to wave flow* $\frac{\tilde{U}_0}{\tilde{u}_0}$. The strength of the barotropic tides relative to the internal wave velocity. For large barotropic tides with rotation, we expect residual currents to develop consistent with tidal-rectification (Loder, 1980; Thomson & Wilson, 1987).
5. *Excursion number,* $Ex = \frac{\tilde{u}_0}{\omega_0 W}$ This can be interpreted as the wave excursion distance to island width and is related to the Keulegan-Carpenter number which describes the relative importance of drag forces to inertia forces. In a stratified fluid, for small Ex, distances traveled by the fluid are smaller than the object scale and turbulence is constrained to near the bottom, while for large Ex values approaching unity, distances traveled by the fluid wave motions are similar to the object scale (Jalali et al., 2014).
6. *Mean flow to wave flow*, $\frac{\overline{U}_0}{\tilde{u}_0}$. A large value implies the solution is dominated by mean barotropic flows, such as mesoscale currents, while a small value approaching zero implies solution is dominated by wave-driven flows.
7. *Barotropic Froude number*, $Fr = \frac{\tilde{u}_0}{C_{BT}} = \frac{\tilde{u}_0}{\sqrt{gH}}$ can be interpreted as the relative importance of the internal wave motions to the barotropic wave speed. For typical oceanic conditions, we expect $C_{BT} \gg \tilde{u}_0$, except in very shallow, highly stratified environments. Thus, this parameter is expected to have low variability for this problem.

8. *Reynolds number* (inertial - viscous): $Re = \frac{\tilde{u}_0^2}{\omega_0 \nu_t}$. This can be interpreted as a wave Re where for large values the flow is highly turbulent as is typical in realistic ocean conditions.

The Barotropic Froude number (7) and Reynolds number (8) are expected to have a limited effect on the variation in flow under the high Re number for realistic oceanic conditions. Thus, for the purposes of this study, we will focus on factors (1) through (6).

2.2. Model Setup

To model internal wave motions and residual currents we employ the SUNTANS model which solves the three-dimensional, nonhydrostatic, Reynolds-averaged Navier-Stokes equations under the Boussinesq approximation, along with the scalar transport equations and the continuity equation (O. B. Fringer et al., 2006). The governing equations are continuity ($\nabla \cdot \boldsymbol{u} = 0$) and the momentum equations, given by

$$\frac{\partial \boldsymbol{u}}{\partial t} + \boldsymbol{u} \cdot \nabla \boldsymbol{u} = -2\boldsymbol{\Omega} \times \boldsymbol{u} - \frac{1}{\rho_0} \nabla p - \frac{g}{\rho_0} \rho \hat{k} + \nabla_H \cdot (\nu_H \nabla_H \boldsymbol{u}) + \frac{\partial}{\partial z} \left(\nu_V \frac{\partial \boldsymbol{u}}{\partial z} \right) + \boldsymbol{F}_M \tag{4}$$

where $\boldsymbol{u} = (u, v, w)$ is the velocity vector in Cartesian coordinates (x, y, z), $\boldsymbol{\Omega}$ is the earth's angular velocity vector, g is gravitational acceleration; (ν, κ, γ) are the eddy-viscosity, eddy thermal diffusivity, and eddy mass diffusivity respectively, $\hat{k}$ is the vertical unit vector, and $()_H$ and $()_V$ are the horizontal and vertical components of a variable or operator. To compute density ρ, an equation of state is employed as a function of temperature T. For density, we assume total density $\rho = \rho_0 + \rho_b(z) + \rho'(x, y, z, t)$, the reference, background, and disturbance density. We can then define the total pressure p as

$$p = q + p_s + g\rho_0(h + r) = q + p_s + g\rho_0 h + \left(p_b + p'\right) = q + p_s + p_{\rho 0} + p_{\rho b} \tag{5}$$

where, following Fringer et al. (2006), we assume p is composed of the nonhydrostatic pressure q, atmospheric pressure p_s, barotropic pressure $\rho_0 g h$, and baroclinic pressure $\rho_0 g r$, where $r = \frac{1}{\rho_0} \int_z^h (\rho_b + \rho')\, dz = \frac{1}{g\rho_0} (p_b + p')$. Similarly, for tracers we define the total, background, and disturbance components as $T = T_b(z) + T'(x, y, z, t)$, and $s = s_b(z) + s'(x, y, z, t)$.

2.2.1. Model Forcing

We employ a nesting model framework (Rogers et al., 2019) to force internal wave motions on the incoming model boundary to a large scale velocity $\boldsymbol{u}_{LS}$, and damp wave motions on the outgoing wave boundary. A horizontal source term in the momentum equations $\boldsymbol{F_M}(x, y, z, t)$ is introduced, such that $\boldsymbol{F_M} = \boldsymbol{F_L} + \boldsymbol{F_D}$ where $\boldsymbol{F_L}$ is the low-frequency forcing and $\boldsymbol{F_D}$ is the sponge layer high-frequency damping term. See Text S1 in Supporting Information S1 for details.

For the Base Case R1, we compute an idealized model simulation of M2 internal tide propagation in one direction based on observations from the South China Sea (Ramp et al., 2010; Zhang et al., 2011). Specifically, we include a typical South China Sea density field (Figures 2a and 2b), with a background temperature profile T_b for stratified summer conditions and for less stratified winter conditions. We set a background passive tracer s_b initial distribution which equals 1 for depths below 100 m (just below the middle mesophotic zone), and equals 0 otherwise (Figure 2c). For most of the depth $f^2 < \omega_{M2}^2 < N^2$, and this environment is capable of sustaining propagating internal waves (Figure 2d). See Text S2 in Supporting Information S1 for additional details.

Boundary conditions ($_{\text{bc}}$) are Dirichlet at the x (East-West) boundaries and periodic in y (North-South). An idealized large-scale velocity field is applied at the model boundary $\boldsymbol{u}_{bc} = \left(\overline{\boldsymbol{U}}_{LS} + \overline{\boldsymbol{u}}'_{LS} + \tilde{\boldsymbol{U}}_{LS} + \hat{\mathcal{F}} \tilde{\boldsymbol{u}}'_{LS} \right) \hat{\imath}_r$ following Rogers et al. (2019) such that,

$$\overline{\boldsymbol{U}}_{LS} = \overline{\boldsymbol{U}}_0 \tag{6}$$

$$\tilde{\boldsymbol{U}}_{LS} = \tilde{U}_0 \frac{\boldsymbol{k}_t}{|\boldsymbol{k}_t|} \cos\left(\boldsymbol{k}_t \cdot \boldsymbol{x} - \omega_{M2} t\right) \tag{7}$$

$$\tilde{\boldsymbol{u}}'_{LS} = \tilde{u}_0 \phi_z \frac{\boldsymbol{k}}{|\boldsymbol{k}|} \cos\left(\boldsymbol{k} \cdot \boldsymbol{x} - \omega_{M2} t\right) \tag{8}$$

where $\tilde{u}_0$ is the boundary horizontal wave amplitude and $\overline{U}_0$ is the boundary mean barotropic motion, $\hat{t}_r$ is a time ramping function, and $\hat{F}(x, y, t)$ selects wave velocities associated with energy flux into the domain. In this study the large-scale, low-frequency baroclinic motions are not applied at the boundary (i.e., $\overline{\boldsymbol{u}}'_{LS} = 0$). Waves in this system consist of both barotropic tides with wavenumber $\boldsymbol{k_t}$ and baroclinic internal tides propagating in the negative x direction with wavenumber $\boldsymbol{k}$ and where ϕ_z is the mode-1 velocity eigenfunction given by solution of the eigenmode problem (Oliver B. Fringer & Street, 2003; Kundu & Cohen, 2008). In the y direction to obtain geostrophic balance in the periodic domain, a forcing $F_{Ly} = -f\,\overline{u}\,\hat{t}_r$ is applied in Equation 4 with a gradual spinup $\hat{t}_r$ to minimize oscillations.

2.2.2. Model Simulations

For the base case R1, we apply this test case on a simplified model of Dongsha atoll as an idealized circular island of width $W = 26$ km, sloping sides with slope $S = 0.05$, surrounded by a domain of constant depth $H = 600$ m, and an effective depth $H_e = 313$ m (Figure 1, Table 1). The bed elevation z_{bot} is given by the equation for a cone, and limited between the maximum depth H and the minimum depth H_{min},

$$z_c = -S\left[(x - x_0)^2 + (y - y_0)^2\right]^{\frac{1}{2}} - H + \text{SR} \tag{9}$$

$$R = \frac{W}{2} + \frac{1}{S}\left(H - \frac{H_e}{2}\right) \tag{10}$$

$$z_{\text{bot}} = \max\left[-H, \min\left(z_c, -H_{\text{min}}\right)\right] \tag{11}$$

where $R(z = -H)$ is the radius of the island at the base, and $W\left(z = -\frac{H_e}{2}\right)$ is taken at $H_e/2$.

We apply this test case on a domain with stretched grid resolution $\Delta x, \Delta y$, which equals 50 m around the island and increases to 1,400 m along the outer boundary and meets the requirements of Vitousek and Fringer (2011) for minimal numerical dispersion when computing the nonhydrostatic pressure. We employ 100 vertical z-levels with enhanced resolution near the surface and exponentially increasing vertical spacing with a growth rate of 1.015, which gives a vertical spacing Δz of 2.6 m at the surface increasing to 11.4 m at maximum depth. For smoothness in the horizontal derivatives, the z-level discretization requires that adjacent horizontal grid points step up/down a maximum of one z level, that is, $\Delta z/\Delta x > S$. For shallow depths in our domain less than 100 m, the majority of effects will be mean flows and diffusion and the model will not resolve the details of turbulence or breaking. For the base case model we employ a constant the kinematic viscosity $\nu = 10^{-3}$ m^2/s in the vertical direction and $\nu_H = 10^{-1}$ m^2/s in the horizontal direction (no turbulence model), and the tracer equations have no specified vertical or horizontal diffusivity (i.e., $\kappa_T = \kappa_s = 0$) similar to values used in other studies at this scale (Kang & Fringer, 2012; Zhang et al., 2011). Central differencing is employed for momentum advection, and the flux-limiting scheme of Casulli and Zanolli (2005) is employed for tracers. The bottom boundary condition is a specified constant drag coefficient $C_D = 0.0025$.

In addition to the base case R1, we conduct a range of simulations (R2–R7, Table 1) meant to explore the response of the residual currents to variations in the important nondimensional factors from Equation 3. Specifically, we look at no rotation (R2), higher Froude number (R3), lower slope (R4), including barotropic tide (R5), higher excursion number (R6), and including barotropic mean flow (R7). Every attempt is made to vary only one parameter from the Base Case (Table 1), but in a few runs this is not possible, such as R4 in which the lower subcritical slope S necessitates a larger width W so that the island top reaches the free surface.

2.2.3. Coordinate Transformation

For this setting where we are interested in the shallow slope region flows on the island, it is convenient to write the model NS equations (Equation 4) in cylindrical coordinates (r, θ, z), where the cross-slope (radial) direction r is directed away from the island center (x_0, y_0), and the along-slope (azimuthal) direction θ is oriented counter-clockwise (Figure 1), the vertical direction z as positive upward, and corresponding

velocity vector $\boldsymbol{u} = (u_r, u_\theta, u_z)$. The transformation is then given by, $x = r\cos\theta + x_0$, $y = r\sin\theta + y_0$, $r = \sqrt{(x-x_0)^2 + (y-y_0)^2}$, $\theta = \arctan\frac{(y-y_0)}{(x-x_0)}$. Similarly, the transformation of velocities can be written as

$$u_r = u\cos\theta + v\sin\theta \tag{12}$$

$$u_\theta = -u\sin\theta + v\cos\theta \tag{13}$$

$$u_z = w \tag{14}$$

Beginning with Equation 4, with nonlinear terms in conservative form, we time average and decompose variables into their high ($\tilde{}$) and low-passed ($\bar{}$) components. Substituting these relationships, expanding the pressure terms, and defining the gradient in cylindrical coordinates as $\nabla \equiv \left(\frac{\partial}{\partial r}, \frac{1}{r}\frac{\partial}{\partial\theta}, \frac{\partial}{\partial z}\right)$, we arrive at the time-averaged momentum equations in cylindrical coordinates in the cross-slope (r) direction

$$\begin{aligned}\left[\frac{\partial\overline{u}_r}{\partial t} + \frac{\partial\overline{u}_r^2}{\partial r} + \frac{1}{r}\frac{\partial\overline{u}_\theta\overline{u}_r}{\partial\theta} + \frac{\partial\overline{u}_z\overline{u}_r}{\partial z} - \frac{\overline{u}_\theta^2}{r}\right] + \left[\frac{\partial\overline{\tilde{u}_r^2}}{\partial r} + \frac{1}{r}\frac{\partial\overline{\tilde{u}_\theta\tilde{u}_r}}{\partial\theta} + \frac{\partial\overline{\tilde{u}_z\tilde{u}_r}}{\partial z} - \frac{\overline{\tilde{u}_\theta^2}}{r}\right] - f\overline{u}_\theta + b\overline{u}_z\cos\theta \\ = -\frac{1}{\rho_0}\frac{\partial\overline{q}}{\partial r} - \frac{1}{\rho_0}\frac{\partial\overline{p}_{\rho 0}}{\partial r} - \frac{1}{\rho_0}\frac{\partial\overline{p}_{\rho b}}{\partial r} + \nu_H\left[\frac{1}{r}\frac{\partial}{\partial r}\left(r\frac{\partial\overline{u}_r}{\partial r}\right) - \frac{\overline{u}_r}{r^2} + \frac{1}{r^2}\frac{\partial^2\overline{u}_r}{\partial\theta^2} - \frac{2}{r^2}\frac{\partial\overline{u}_\theta}{\partial\theta}\right] \\ + \nu_v\frac{\partial^2\overline{u}_r}{\partial z^2} + \overline{F}_r\end{aligned} \tag{15}$$

and in the along-slope (θ) direction,

$$\begin{aligned}\left[\frac{\partial\overline{u}_\theta}{\partial t} + \frac{\partial\overline{u}_r\overline{u}_\theta}{\partial r} + \frac{1}{r}\frac{\partial\overline{u}_\theta^2}{\partial\theta} + \frac{\partial\overline{u}_z\overline{u}_\theta}{\partial z} - \frac{\overline{u}_r\overline{u}_\theta}{r}\right] + \left[\frac{\partial\overline{\tilde{u}_r\tilde{u}_\theta}}{\partial r} + \frac{1}{r}\frac{\partial\overline{\tilde{u}_\theta^2}}{\partial\theta} + \frac{\partial\overline{\tilde{u}_z\tilde{u}_\theta}}{\partial z} - \frac{\overline{\tilde{u}_r\tilde{u}_\theta}}{r}\right] + f\overline{u}_r - bu_z\sin\theta \\ = -\frac{1}{\rho_0 r}\frac{\partial\overline{q}}{\partial\theta} - \frac{1}{\rho_0 r}\frac{\partial\overline{p}_{\rho 0}}{\partial\theta} - \frac{1}{\rho_0 r}\frac{\partial\overline{p}_{\rho b}}{\partial\theta} + \nu_H\left[\frac{1}{r}\frac{\partial}{\partial r}\left(r\frac{\partial\overline{u}_\theta}{\partial r}\right) - \frac{\overline{u}_\theta}{r^2} + \frac{1}{r^2}\frac{\partial^2\overline{u}_\theta}{\partial\theta^2} - \frac{2}{r^2}\frac{\partial\overline{u}_r}{\partial\theta}\right] \\ + \nu_v\frac{\partial^2\overline{u}_\theta}{\partial z^2} + \overline{F}_\theta\end{aligned} \tag{16}$$

where the Coriolis effect in the horizontal $f = 2\Omega\sin\varphi$, and vertical $b = 2\Omega\cos\varphi$ directions, ϕ is latitude and $\Omega = 7.27 \times 10^{-5}$ rad/s.

3. Results and Discussion

To evaluate how internal tides influence the shallow slope region flows, we conduct a series of simulations (Table 1) beginning with an idealized Dongsha Atoll under summer stratification conditions (R1). We explore the internal wave and mean flow dynamics using the time-averaged momentum equations and then explore the effects of variations on different important parameters on the mean flows, upwelling, and ecologically relevant parameters.

3.1. Internal Tides

3.1.1. Wave Dynamics

Internal tides applied at the model boundary steepen as they travel through the model domain (Figure 1c) and approach the island as solitary-like nonlinear internal waves. The free surface η normalized by depth H_e shows the internal waves approaching the island from the right as a single defined wave for Base Case R1 (Figure 3a). As the wave encounters the island, the waves on the north and south sides of the island refract around the island and are slower in the shallow regions (Figures 3b–3g), and some reflections are visible on the eastern side of the island (Figure 3e). The wave form changes as it propagates to shallow depths, where on the eastern side of the island at the bottom of the slope, the waveform is a wave of depression in temperature and velocities are quite smooth (Figures 4a, 4c, and 4e, 4g), while at the shallow slope the waveform is a nonlinear wave of elevation in temperature with complex velocities (Figures 4b, 4d, and 4f, 4h). Wave motions are strongest in the direction of wave propagation (u_r), but also present in the azimuthal direction (u_θ) due to the effects of rotation (Figures 4e–4g, and 4h). At 30 m depth in the x-y plane, the velocity field shows strong velocities directed in the $-x$ direction for

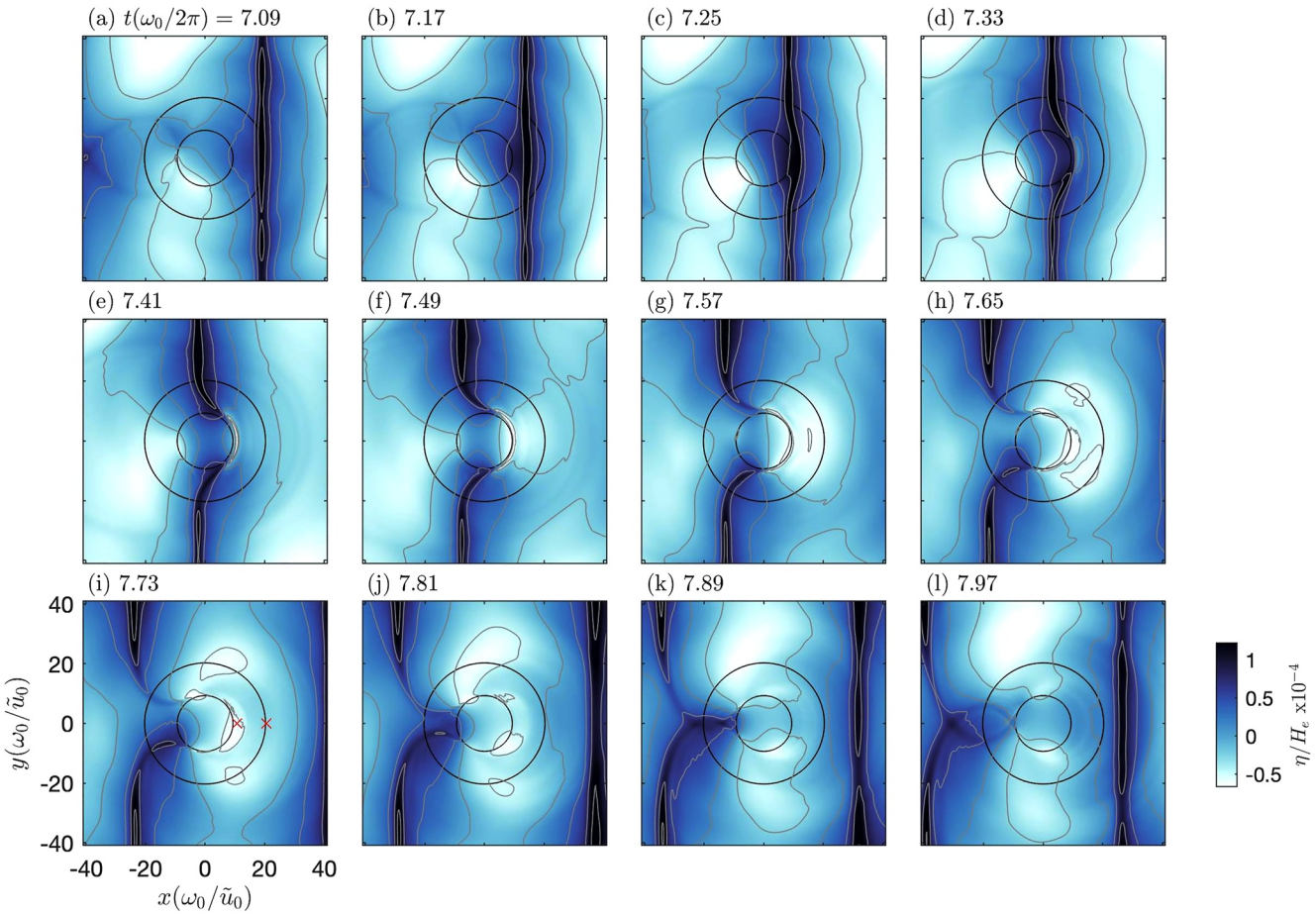

Figure 3. Wave propagation from right to left and interaction with the island for Base Case R1, showing the normalized free surface η/H_e over one wave period. Times shown are from start of simulation, black lines show upper and lower extent of island slope, gray lines show equal contours of η/H_e.

the offshore wave approaching from the right, while the shallow slope region velocities are generally directed in a clockwise sense and in the x-z plane the depth variability of density shows the offshore wave is a wave of depression associated with decreased density near the surface (Figure S1 in Supporting Information S1). As the wave approaches the west side of the island, the wave amplitude on the south side is enhanced and has traveled slightly further than the wave on the north side in the shallow slope region (Figures 3h–3j). The wave nearly leaves the field of view to the west as the next wave approaches (Figures 3k–3l).

The basic mechanism for wave transformation is as follows, illustrated using the first wave arriving at the island (Figure 5),

1. The wave approaches the island with a symmetric wavefield (Figure 5a). The wave speed C is slower in shallow water than the deeper areas with speed C_0, due to changes in H_e. As the wave propagates, refraction bends the wave toward the shallow depths due to differences in C and bottom friction. As the wave velocities wrap around the curved island with variations in bottom stress due to the sloping bottom (Signell & Geyer, 1991), this induces a vorticity ω_z, which is acting in concert with rotation f on the left side of the propagating wave (A_{crest}), while acting opposite to rotation f on the right side (B_{crest}) (for this example in the northern hemisphere). Note that the wave crest in the free surface is associated with a depression of the temperature at the deep slope (Figures 4a and 4c), and a complex nonlinear form in the shallow slope (Figures 4b and 4d).
2. As the wave refracts to propagate normal to the coastline, the effect of rotation becomes important (Figure 5b). The wave crest has a negative velocity $\tilde{u}$ (in the x direction), which implies the Coriolis force acts in the positive y direction ($-f\tilde{u}$). On the south side this force acts to enhance the positive y pressure gradient, and create a larger wave amplitude at point A_{crest}. On the north side, the opposite occurs: the Coriolis force acts opposite to the y pressure gradient, creating a smaller wave amplitude at point B_{crest}.

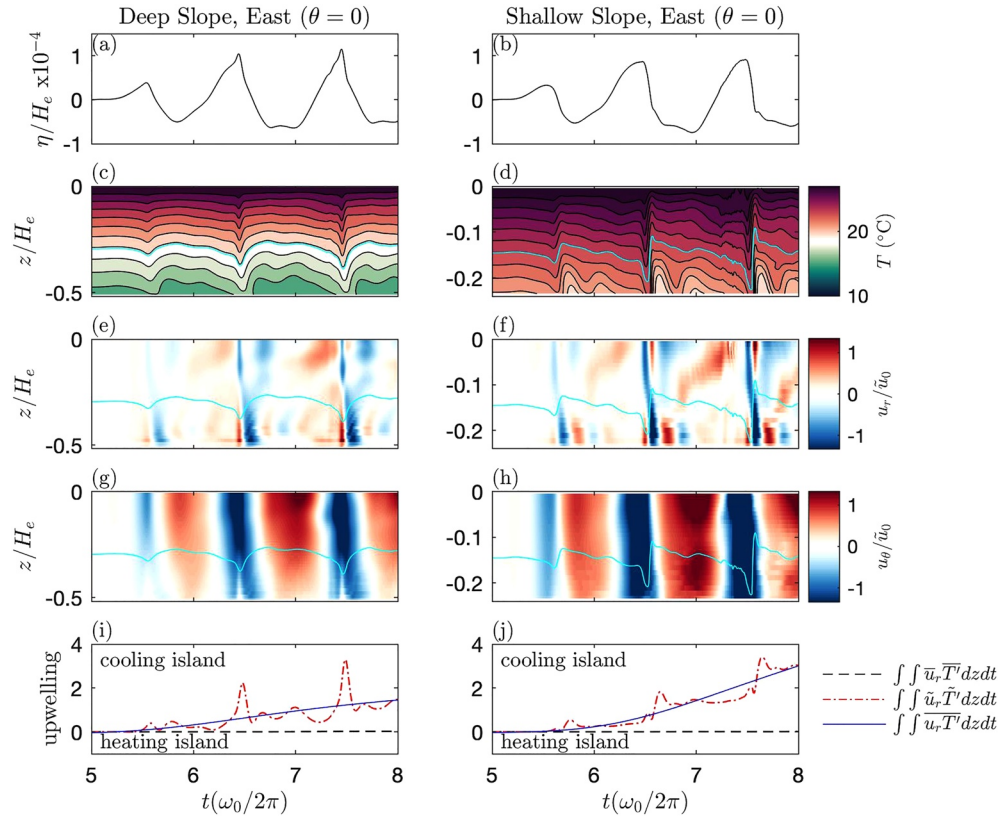

Figure 4. Wave propagation and heat transport in time on the eastern side of the island ($\theta = 0$) for Base Case R1 at the deep slope (left) and shallow slope (right) showing (a and b) free surface η/H_e, (c and d) temperature T, (e and f) velocity in r direction u_r (g and h) velocity in θ direction u_θ, and (i and j) net cumulative heat transport in cross-slope direction (upwelling) comparing mean advection, wave advection, and total average advection terms ($m^2{}^\circ C s^{-1} \times 10^4$). Location of left and right shown in Figure 3 with depth 161 and 72 m, respectively. Note the vertical scale in (c, e, and g) is different than (d, f, and h) due to the different depth at each location. For (i and j) integrals in z are over the bottom of the water column ($\int_{-H}^{\zeta_0} dz$) where ζ_0 is a line of constant density shown by cyan line in (c–h).

3. When the wave crest has nearly wrapped around the island, the wave at point A_{crest} on the southwest side is has larger velocities by a factor of two and is broader in extent than point B_{crest} on the northwest side (Figure 5c). The main wave crest is beginning to separate from the portion of the wave wrapping around the island. At this point B_{trough}, the wave trough has a positive $\tilde{u}$ velocity. On the south side this force enhances the negative y pressure gradient creating a deeper wave trough at A_{trough}. On the north side, the opposite occurs. The Coriolis force acts in the negative y-direction, damping the wave trough at B_{trough}.
4. Finally, the next wave approaches the island from the east and is symmetric (Figure 5d). The remnant wave from the left side of the island (A_{crest}, A_{trough}) continues to propagate around the island in a clockwise direction. This wave will encounter the next wave propagating in the opposite direction, possibly leading to destructive interference. The remnant wave from the right side of the island (B_{crest}) is not visible and has nearly dissipated. Thus, the next wave will encounter no opposing waves on the south side.

These results indicate that the primary influence on the wavefield is differences in depth leading to differential travel speeds and refraction, and on whole are similar to previous modeling studies (Chao et al., 2006; Masunaga et al., 2017). In the absence of rotation (No Rotation R2, Table 1), the wavefield is significantly different than the base case R1 (Figure 6). The waves are separated into more nonlinear peaked shapes with trains of ranked order solitary waves, wave amplitudes are larger and the wave velocities in the direction of propagation (u_r) are stronger (Figure S2 in Supporting Information S1). Without rotation effects, the wavefield is symmetric about the x axis at the island center, reflections are more apparent (Figures 6j–6l), and on the eastern side of the island velocities in the azimuthal direction (u_θ) are very weak (Figure S2 in Supporting Information S1). These results are consistent with previous work which found rotational dispersion causes internal waves to travel faster and

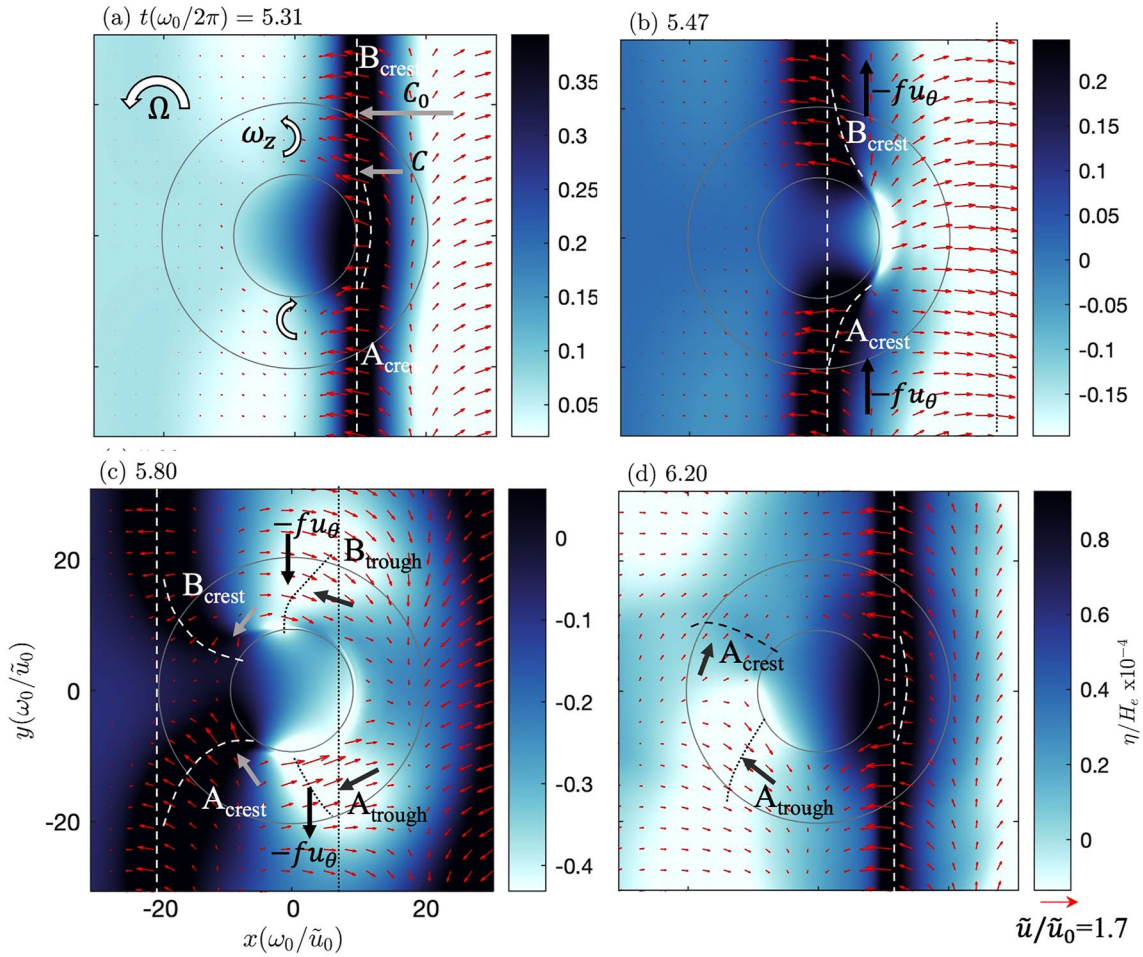

Figure 5. Mechanism for wave interaction with the island and formation of asymmetric waves, showing the normalized free surface η/H_e and wave velocities $\tilde{u}/\tilde{u}_0$ for Base Case R1. (a) Wave approaches the island from the east in a rotating frame Ω. (b) As wave reaches midpoint of island, point A_{crest} is acted upon by Coriolis force toward the island center, amplifying the wave, while point B_{crest} is subject to a force away from the island center damping the wave amplitude. (c) Wave reaches the western side of the island. (d) As the next wave approaches from the east, the remnant wave at point A_{crest} continues to wrap around the island. Note white arrows indicate rotation, gray arrows indicate feature movement, black arrows indicate force direction, dashed lines indicate wave crest (--) and trough (..) location, red lines indicate wave velocity at $z = -30$ m, and gray solid lines indicate upper and lower extent of island slope.

reduce the effects of steepening (Farmer et al., 2009; Helfrich, 2007). Diffraction patterns are also apparent (Figures 6a–6e) (diffraction being the bending of waves around a sharp object). However, distinguishing the importance of refraction versus diffraction in this case is challenging and a potential avenue for future study. The remaining cases R3–R7 have wave characteristics quite similar to R1, with some small variations, and thus are not explored in detail.

3.1.2. Wave Effects

The result in Equation 3 represents a set of independent variables governing the problem. By combining them, additional understanding can be gained into the system dynamics. One such parameter governing Kelvin wave resonance and scattering is $Fr\,Ex^{-1}/2\pi = \frac{W}{\lambda_0}$, which is a measure of the island width to wavelength. For values of $Fr\,Ex^{-1}/2\pi$ greater than one, island width is larger than the wavelength and refraction should dominate, while for values less than one, diffraction should dominate. For the base case R1, $FrEx^{-1}/2\pi = \frac{W}{\lambda_0} = 0.375$, where the island width is a similar scale as the internal wavelength and we expect both refraction and diffraction to occur. Refraction is apparent in the waves wrapping around the island for case R1 (Figure 3). Diffractive patterns are not significant for case R1 but are apparent in the no rotation case R2 (Figure 6). For smaller values of $FrEx^{-1}$

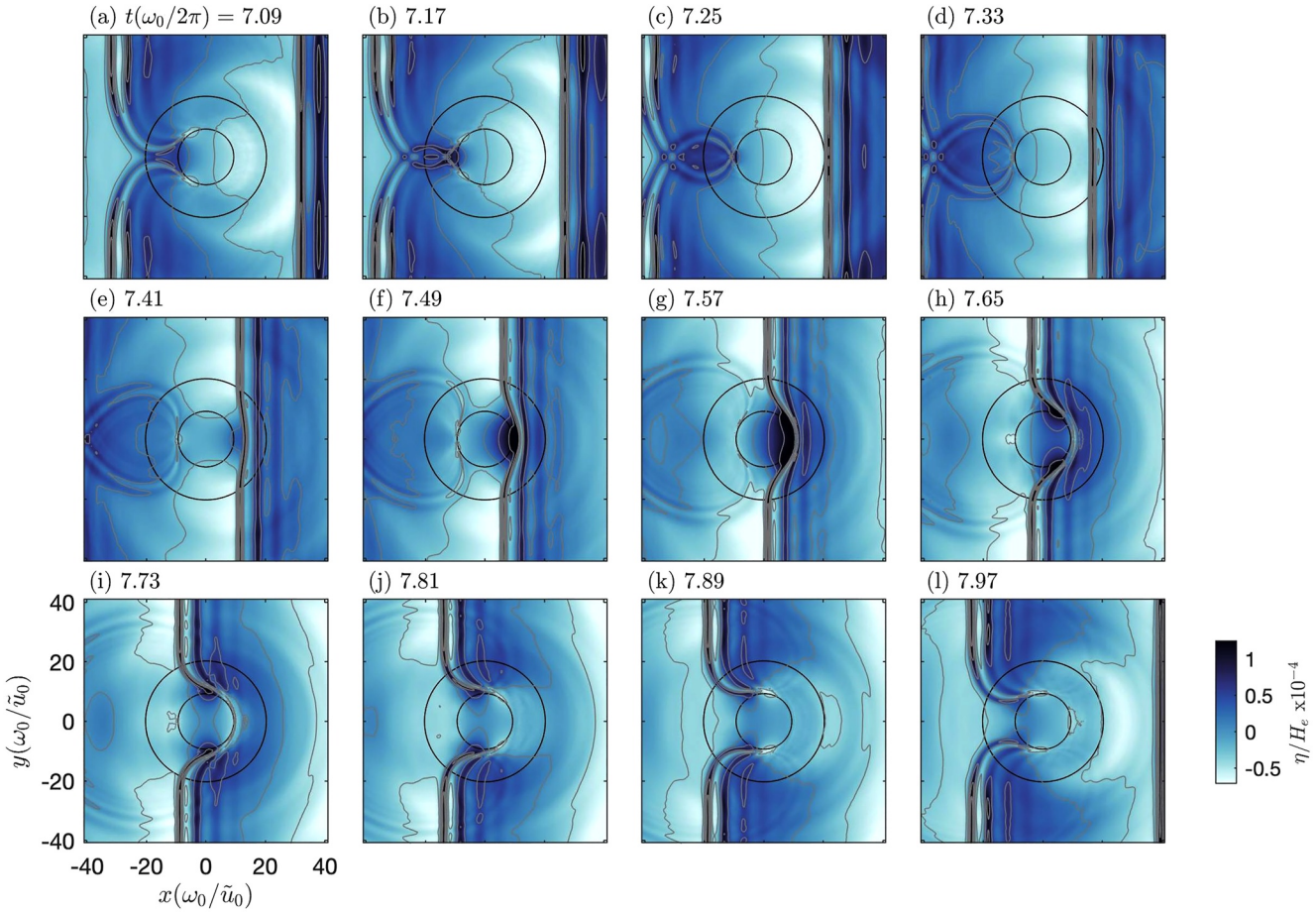

Figure 6. Wavefield progression for No Rotation Case R2, showing normalized free surface η/H_e over one wave period. Times shown are from the start of the simulation, while black lines show upper and lower extent of island slope, gray lines show equal contours of η/H_e.

approaching zero, we would expect complex scattering patterns to become apparent. Studying those diffractive processes is beyond the scope of this study.

Additionally, we can estimate the Kelvin wave frequency $\omega_k = 2\pi\frac{C_k}{L_c}$ from the mode one internal wave speed around the island (Masunaga et al., 2017), where the circumference $L_c = \pi W$ and the Kelvin internal wave speed near the island $C_k = \frac{C_0}{2}$ is taken at depth $H_e/2$. Substituting these we can rewrite, $FrEx^{-1} = \frac{\omega_0 W}{C_0} = \frac{\omega_0}{\omega_k}$. Internal Kelvin wave resonance can occur when the incoming wave frequency ω_0 is close to n integer multiples of the Kelvin wave frequency ω_k. For Kelvin waves rotating faster than the incoming waves, resonance occurs at $FrEx^{-1} = \frac{1}{n}$. For Kelvin waves rotating more slowly than the incoming waves, the two waves meet at n integer values of $FrEx^{-1}$, but their interaction is complicated by destructive interference when the kelvin wave traveling around the island encounters the next incoming wave when $FrEx^{-1} = n_{\text{even}}$. In this case, strong resonance only occurs at $FrEx^{-1} = n_{\text{odd}}$. Thus, we expect resonance to occur when,

$$\omega_0 > \omega_k,\ \text{FrEx}^{-1} = \frac{1}{n}, \tag{17}$$

$$\omega_0 \leq \omega_k,\ \text{FrEx}^{-1} = n_{\text{odd}}$$

The results also show that the wavefield is influenced by rotation in two ways. The first, and most important, is the Kelvin wave effect where in the northern hemisphere, wave motions traveling along a right curved boundary are enhanced, while those traveling along a left curved boundary are damped. For this example case, since the

time-scale of the wave passing the island is smaller than the inertial period, the Kelvin wave does not have time to fully adjust to the dynamics (Liu et al., 1999). Nevertheless, the mechanism has a significant effect on inducing asymmetry to the wavefield.

The second rotational mechanism relates to remnant Kelvin waves traveling around the island in the clockwise direction, which provide destructive interference with incoming waves. In this case the rotating Kelvin waves exist at a lower frequency than the incoming waves ($\omega_0 \leq \omega_k$). Therefore, we expect resonance to occur when $FrEx^{-1} = n_{\text{odd}}$. For case R1, $FrEx^{-1} = 2.24$, which is not close to the resonant condition requiring odd values of n. In case R1, the Kelvin waves wrap around the island and are located at approximately the northwest corner when the next wave is approaching, and thus resonant effects are minimal (Figure 5d). However, under different conditions, this effect could be important in creating resonance (Masunaga et al., 2017).

While not the focus of this study, the fate of internal tide energy is of relevance to this problem. Previous studies of Dongsha Atoll have noted approximately 20% of the incident wave energy is reflected (Bai et al., 2017; Davis et al., 2020), which should be quite similar for the base case R1. The slope criticality α is expected to be a primary control on this, and for subcritical slopes as in case R4, we expect a high percentage of the internal tide energy to be dissipated (Hall et al., 2013). In addition, we hypothesize if we simulated adding barotropic tides and subcritical slopes to case R1 (i.e., combine R4 and R5) that local internal tides would be generated from the island, a potential topic for future work.

A related parameter to α is the internal Iribarren number $\xi = S\left(\frac{a_0}{\lambda_0}\right)^{-\frac{1}{2}} \approx Fr^{-2}S$ (Boegman et al., 2005), where a_0/λ_0 is a measure of the internal tide nonlinearity and proportional to Fr. While ξ is an appropriate classifier for internal tides, which have long wavelengths relative to their amplitude, it is important to note its limitations in classifying internal solitary wave breakers, which generally have shorter wavelengths and thus steeper wave slopes a_0/λ_0 (Masunaga et al., 2019). In particular, ξ does not necessarily uniquely define internal solitary wave properties, such as breaker type or mixing efficiency, for a given wave and topographic slope; it is therefore more appropriate to classify internal solitary wave breaking in terms of α (Masunaga et al., 2019).

3.2. Residual Flows

3.2.1. Residual Flow Dynamics

The central question for this section relates to the mechanism by which mean residual currents are created, with a focus on the sloping island sides for depths less than H_e. To understand the mechanism driving the currents, we begin with the time-averaged momentum equations, transformed to cylindrical coordinates (Equations 15 and 16) and then simplified to retain only the significant terms of dynamic importance. In the present simulations, no low-frequency forcing was applied so $\overline{F}_r = \overline{F}_\theta = 0$, and the surface pressure $p_s = 0$. Based on model results of the base case R1, the material derivative of the mean flow ($D\overline{u}/Dt$), mean nonhydrostatic pressure, Coriolis forcing from vertical motions, and horizontal turbulent diffusion terms are all negligible and less than 1×10^{-7} m/s^2. Thus, the cross-slope and along-slope momentum equations can be approximated by

$$\left[\frac{\partial \overline{\tilde{u}_r^2}}{\partial r} + \frac{1}{r}\frac{\partial \overline{\tilde{u}_\theta \tilde{u}_r}}{\partial \theta} + \frac{\partial \overline{\tilde{u}_z \tilde{u}_r}}{\partial z} - \frac{\overline{\tilde{u}_\theta^2}}{r}\right] - f\overline{u}_\theta = -\frac{1}{\rho_0}\left[\frac{\partial \overline{p}_{\rho 0}}{\partial r} + \frac{\partial \overline{p}_{\rho b}}{\partial r}\right] + \nu_v \frac{\partial^2 \overline{u}_r}{\partial z^2} \tag{18}$$

$$\left[\frac{\partial \overline{\tilde{u}_r \tilde{u}_\theta}}{\partial r} + \frac{1}{r}\frac{\partial \overline{\tilde{u}_\theta^2}}{\partial \theta} + \frac{\partial \overline{\tilde{u}_z \tilde{u}_\theta}}{\partial z} - \frac{\overline{\tilde{u}_r \tilde{u}_\theta}}{r}\right] + f\overline{u}_r = -\frac{1}{\rho_0 r}\left[\frac{\partial \overline{p}_{\rho 0}}{\partial \theta} + \frac{\partial \overline{p}_{\rho b}}{\partial \theta}\right] + \nu_v \frac{\partial^2 \overline{u}_\theta}{\partial z^2} \tag{19}$$

respectively. For both equations, the terms are the radiation stress gradients (RSG1, RSG2, RSG3, RSG4), horizontal Coriolis force (Cor1), barotropic and baroclinic hydrostatic pressure gradients ($\text{PGh}_{\rho 0}$, $\text{PGh}_{\rho b}$), and vertical turbulent diffusion (DissV).

The time-averaged wave oscillatory motions $\overline{|\tilde{u}^2|}/\tilde{u}_0^2$ scales like the radiation stresses and are helpful for understanding the average wave behavior and regions of strong RSG forcing for cases R1–R7 (Figure 7). Most of the cases show asymmetric average wave fields consistent with the effects of rotation with case R5 (barotropic

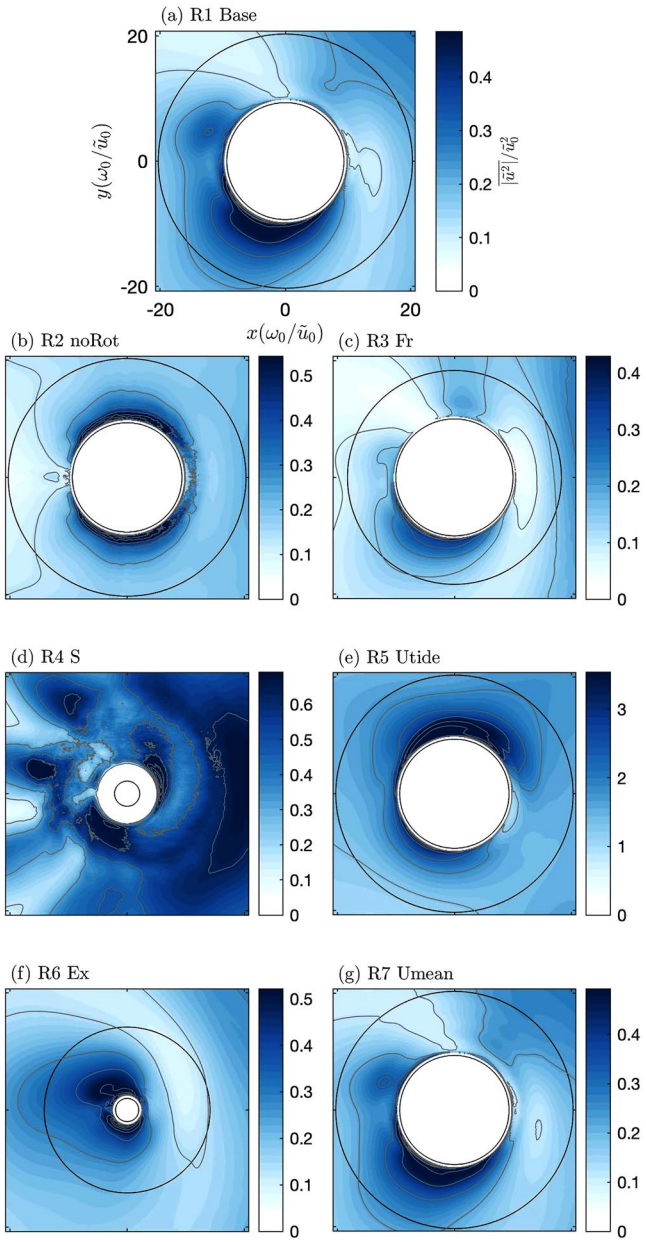

Figure 7. Average wave oscillatory motions $|\overline{\tilde{u}^2}|/\tilde{u}_0^2$ for different simulations R1–R7 from top view (x, y) along a z plane $z/H_e = -0.09$ (see Figure 9 for location), black lines show upper and lower extent of island slope, gray lines are contours of wave oscillatory motions. Note the color scales vary in each panel, and horizontal scales are normalized by $\tilde{u}_0/\omega_0$, where the absolute scale of island is given by W in Table 1. For R4, the lower island slope is outside the field of view.

tide) having the largest magnitude (Figure 7e), while case R2 (no rotation) is symmetric along the x axis (Figure 7b). The subcritical slope case R4 regions of enhanced wave motions are more evenly distributed around the island compared to case R1 (Figure 7d).

The residual currents vary in magnitude and direction for the different cases R1–R7 (Figures 8 and 9). The mean currents are typically enhanced in areas of strong gradients in radiation stress (Figure 7) and most have some component of clockwise rotation (Figure 8). In contrast, case R2 (no rotation) currents are symmetric about the x-axis (Figure 8b). The cases with the largest magnitude of currents are case R4 (low slope), case R5 (barotropic tide) and case R7 (barotropic mean flow) (Figures 8d, 8e, and 8g). There is vertical variability in the currents, with cross-slope flow dependent on depth, and for most cases the strongest flows are below the surface near a depth of $\frac{z}{H_e} \sim 0.15$ (Figure 9).

The mechanism for generation of the mean flows can be explained by analyzing the depth-integrated momentum terms in Equations 18 and 19 along a transect at the southeast corner of the island (Figure 10). For simplicity we evaluate the Base Case R1, as well case R2 (no rotation) and case R7 (barotropic mean flow), which cover changes to the primary external forcing (waves, rotation, and barotropic pressure gradients).

1. The primary forcing mechanism is the incoming internal waves which shoal, break, refract, and diffract around the island creating gradients in the Radiation stresses in both the cross-slope and along-slope directions (RSG1–RSG4) (Figure 7). For case R1 and R7, the strongest wave motions are on the southwest corner of the island, while for case R2 wave motions are symmetric. Different forcing and geometric conditions change this spatial pattern (Figures 7c–7f).
2. In the cross-slope r direction (Equation 18) the Radiation stress gradients drive a barotropic pressure gradient which is balanced by a baroclinic pressure gradient and the Coriolis force for case R1 (Figure 10d), which accelerates flow $\overline{U}_\theta$ in the along-slope θ direction (Figure 10a). Additionally, a small contribution from the vertical turbulent diffusion is associated with flow $\overline{U}_r$ in the cross-slope direction. For the no rotation case R2, the balance of terms is similar to R1 but without the Coriolis force (Figure 10e), and magnitudes of velocities are larger than case R1 (Figure 10b). For case R7, the barotropic pressure, baroclinic pressure and Coriolis force terms are larger than case R1 (Figure 10f), and the magnitudes of velocities are significantly larger (Figure 10c).
3. In the along-slope θ direction (Equation 19), Radiation stress gradients induce a barotropic pressure gradient, the Coriolis force, and a smaller contribution from the vertical turbulent diffusion (Figure 10g). Note the magnitude of momentum terms is smaller in the θ direction than in the r direction. For the no rotation case R2, the balance of terms is similar to R1 but without the Coriolis force (Figure 10h), and magnitudes of velocities are larger than case R1 (Figure 10b). For case R7, the barotropic pressure, baroclinic pressure and Coriolis force terms are larger than case R1 (Figure 10i), and the magnitudes of velocities are significantly larger (Figure 10c).

Thus, spatial changes in wave motions generate along-slope mean flows $\overline{U}_\theta$ through two mechanisms: (a) the turbulent diffusion term in the along-slope direction equation (DissV, Equation 19) forced by along-slope gradients in the wavefield and (b) through the Coriolis term (Cor1, Equation 18) in the cross-slope direction equation

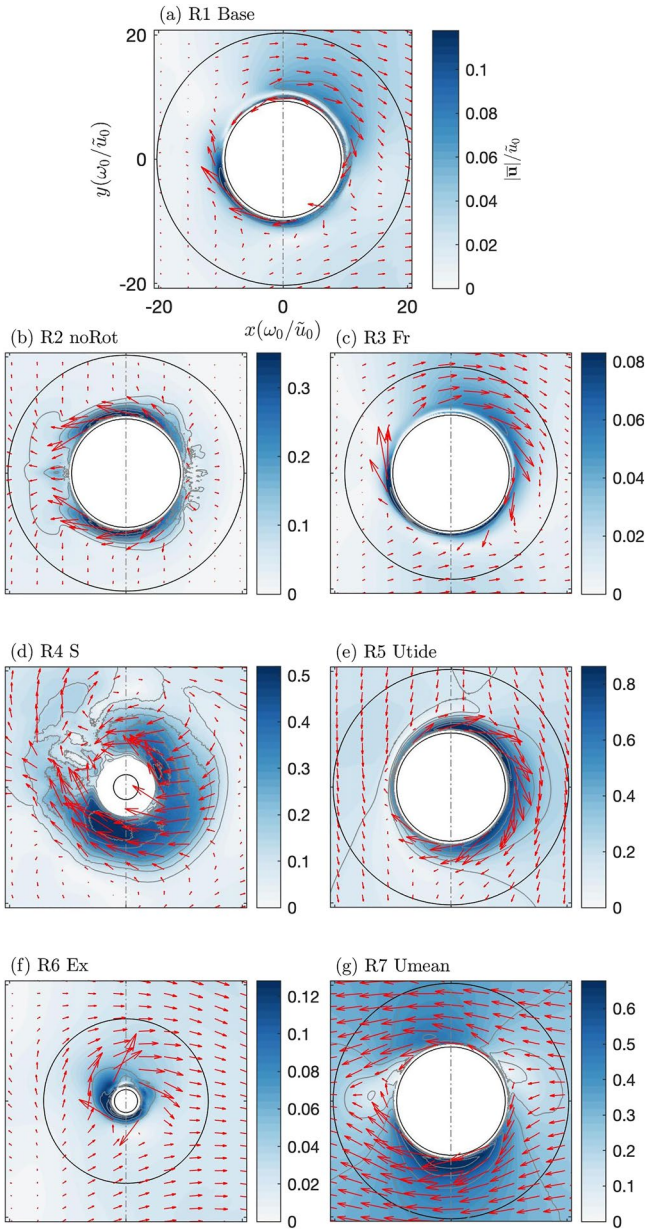

Figure 8. Average residual flows $|\overline{u}|/\tilde{u}_0$ for different simulations R1–R7 from top view (x, y) along a z plane $z/H_e = -0.09$ (see Figure 9 for location). Maximum vector scale corresponds to the maximum color bar value, black lines show upper and lower extent of island slope, gray lines are contours of residual flows. Note the color scales vary in each panel, and horizontal scales are normalized by $\tilde{u}_0/\omega_0$, where the absolute scale of island is given by W in Table 1. For R4, the lower island slope is outside the field of view.

forced by cross-slope gradients in the wavefield. The pressure gradient terms serve as additional balancing terms, which tend to be spatially smooth, and are enhanced by other external barotropic forcing as in the barotropic mean flow case.

3.2.2. Residual Circulation Drivers

We conducted simulations to understand the factors that drive residual currents in the shallow slope regions of an island by comparing different forcing scenarios. The mechanism for generating residual currents has been explored in the previous section and essentially relates to spatial gradients in the wavefield which are caused by the wave interaction with the bathymetry and Coriolis forcing (if present). The detailed wave and mean flow physics for each case R1–R7 are complex and investigation of each is beyond the scope of this work. For this work, we focus on the potential for enhanced residual currents from the different factors.

The results of cases R2–R7 indicate that the most important factors for generating larger magnitude residual flows in the shallow slope region compared to R1 are no rotation (R2), reduced slope S below the critical value (R4), offshore barotropic tidal forcing (R5), and offshore barotropic mean flow forcing (R6). These trends are apparent in the near-bottom mean velocities in the shallow regions around the island (Figure 12b), as well as the barotropic mean velocities (Figure S3 in Supporting Information S1). The mean currents in case R3 (higher Fr) and case R6 (higher Ex) are similar to case R1, and thus are not explored in detailed here. It is important to note that Fr in case R3 (taken at the deep water location) is only 41% higher than in case R1, while in field conditions, we would expect a very wide range of Fr in deep waters. A topic for future work could be to explore this variability with Fr further.

The no rotation case (R2) significantly changes the nature of the internal waves to be more nonlinear through lack of rotational dispersion and produces a symmetric wavefield around the island (Figure 6). Additionally, the mechanism for residual current generation no longer includes Coriolis forcing and relies on the vertical turbulent diffusion term in the along-slope direction (Section 3.2), which forces mean flows in the direction of wave propagation. Thus, the effect of no rotation is to change the direction of residual flows and increase the magnitude compared to case R1. Taken broadly, we expect residual flows on islands near the equator to resemble case R2, while islands located at mid-latitudes to resemble case R1. For islands located toward the poles where $Ro < 1/2\pi$, all wave motions become inertial, and other dynamics would dominate than are covered here. For islands located poleward of critical latitudes for M2 and K1 tides, waves are coastally trapped (Masunaga et al., 2017).

The low bathymetric slope case (R4) reduces the slope S to a subcritical regime ($\alpha < 1$), where we expect wave energy to propagate onshore and dissipate (Eriksen, 1982; Lamb, 2013), in contrast to case R1 which has a supercritical slope. The shallow slope region wavefield is enhanced compared to R1, and flow directions are similar to R1 with clockwise directed flow, but the flow on the north side of the island is reversed and directed in the direction of wave propagation. Thus, the primary effect of a subcritical slope is to enhance wave breaking and thus significantly increase the residual currents, here by a factor of five. At a global scale, we would thus expect islands with subcritical slopes to see significantly larger residual flows. While the present study assumes a smooth idealized bathymetry, natural island geometries have variability at a wide range of scales. Previous work has found that on supercritical slopes, local patches of subcritical slopes can force strong currents, and the slope can dissipate significant wave energy (Hall et al., 2013). Thus, an area of future work

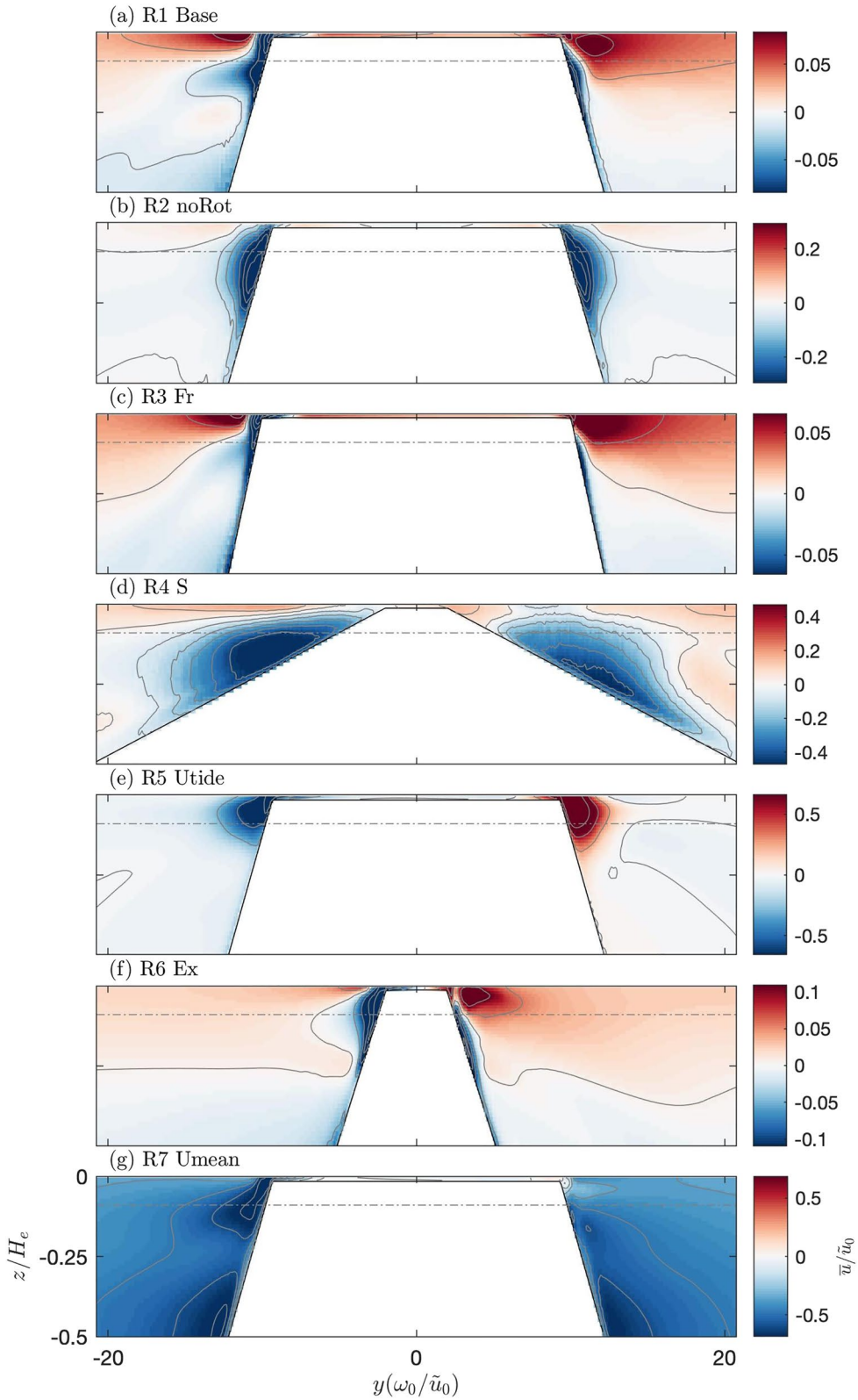

Figure 9. Residual flows $\overline{u}/\tilde{u}_0$ in the x-direction for different simulations R1–R7 from N/S side view (y, z), where internal tides are propagating into the figure in this view (see Figure 8 for location), gray lines are contours of residual flows. Note the color scales vary in each panel, and horizontal scales are normalized by $\tilde{u}_0/\omega_0$, where the absolute scale of island is given by W in Table 1.

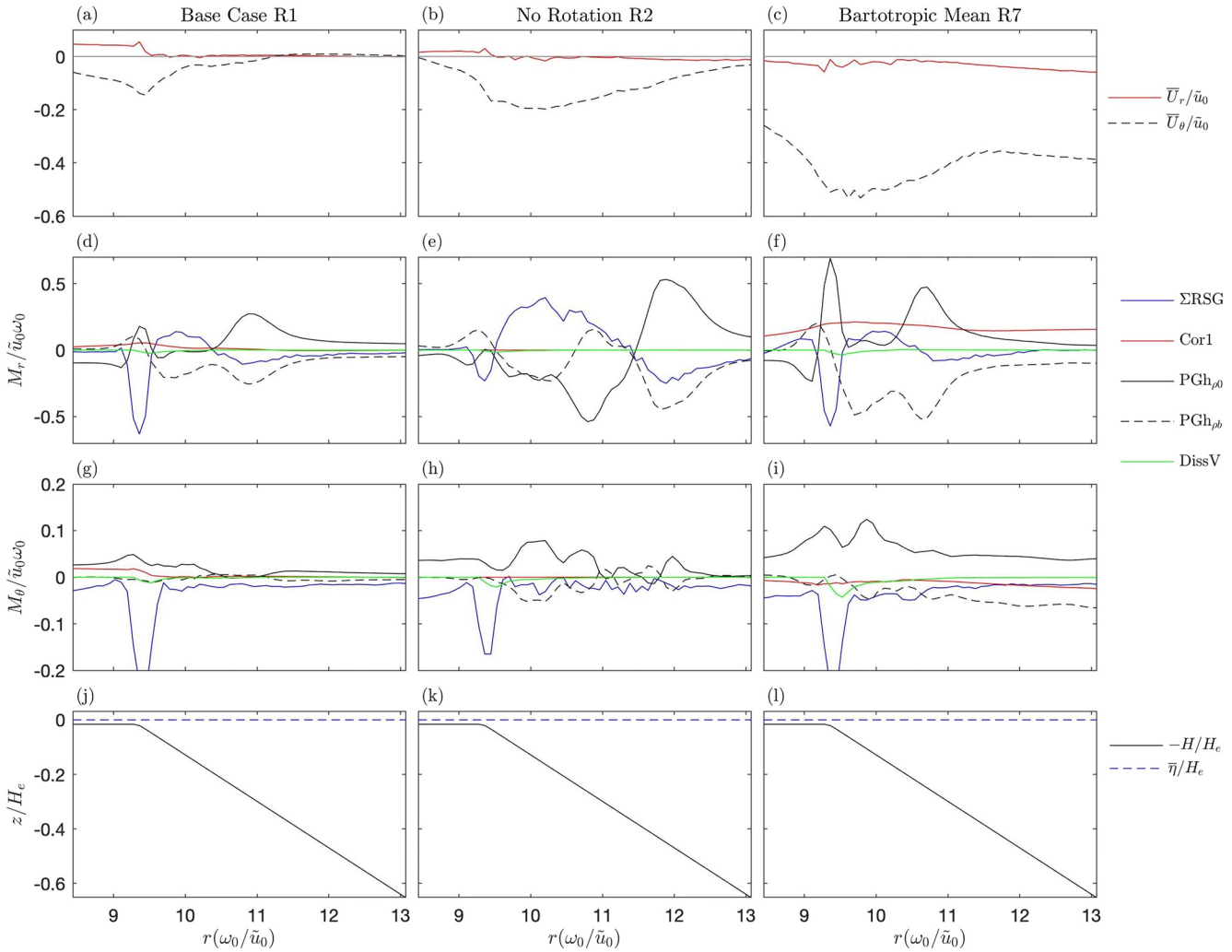

Figure 10. Depth-integrated time-averaged momentum balance profiles for base case R1 (left), no rotation case R2 (center) and barotropic mean flow case R7 (right) at the southeast ($\theta = -45°$) side of the island showing (a–c) cross-slope and along-slope average barotropic velocities ($\overline{U}_r/\tilde{u}_0, \overline{U}_\theta/\tilde{u}0$) (d, e, f) cross-slope depth-averaged momentum balance terms M_r from Equation 18, (g–i) along-slope depth-averaged momentum balance terms M_θ from Equation 19, and (j–l) bathymetry ($-H/H_e$) and free surface ($\overline{\eta}/H_e$).

would be to characterize the importance of local bathymetry variability at a range of spatial scales on the formation of residual currents.

The residual mean flows generated by the addition of barotropic tides (R5) are the largest of any of the tested scenarios, with flows directed in the clockwise direction. In this case, Coriolis forcing has a strong effect, and residual Kelvin waves are generated by the incoming barotropic waves, which propagate around the island in a clockwise direction. As these waves dissipate, they generate residual currents. This effect has been well studied and is often referred to as tidal-rectification (Loder, 1980; Thomson & Wilson, 1987). The scale of the island has an effect here, where island of scale near the Rossby radius ($L_R = \frac{NH_e}{f} = \frac{C_0}{f}$) would see the largest effect because the curvature of the island matches the curvature induced by rotation. If we divide this scale by the island width scale, this is a form of the Burger number (Bu), which can also be expressed in terms of the terms in Equation 3, $Bu = \frac{L_R}{W} = RoFr^{-1}Ex$. The physical interpretation is the ratio of stratification to rotational effects, where for small Bu we expect rotation to dominate while for large Bu stratification dominates. For the base case (R1) and most of the model scenarios, Bu is close to one, while the low slope case (R4) has the smallest value (indicating rotation is important), while the higher excursion number case (R6) has the largest value (indicating stratification is important) (Table 1).

In case R5, phasing of arriving internal waves at the eastern edge of the island was approximately when the barotropic tide was falling. The effectiveness of this mechanism in driving currents is likely dependent on the phase difference between the barotropic and internal tide forcing applied at the model boundary, an effect which was not explored in this work. Globally, barotropic tide forcing varies significantly, and we would expect islands within regions of strong tidal forcing to see the largest barotropic residual currents.

Finally, flows generated by large-scale barotropic currents (R7) are similar to uniform flow around a cylinder, but with some modification from the wavefield which creates an asymmetry in the flow field (Figure 8g). The resulting mean flows are to the west around the island, but with enhanced velocities on the southern side of the island and an asymmetry in the flow where the southern 2/3 of the island has clockwise flow and the northern ⅓ of the island has counterclockwise flow. The magnitude of the residual flow in the shallow slope region is about twice that of the applied offshore mean flow ($\overline{u}/\tilde{u}_0 \sim 2$) because of the internal wave forcing and impinging mean flow as it accelerates around the island. Globally, flows of scales much larger than islands are common, typically arising from large-scale ocean currents, mesoscale eddies, and other features whose magnitude can vary greatly. Thus, in regions of strong large-scale currents, we would expect flows similar to case R7.

3.3. Upwelling

3.3.1. Upwelling and Temperature Dynamics

The movement of water affects the temperature through advective transport (*i.e.*, $\nabla \cdot \overline{uT'}$). In the context of this study, we define upwelling as the near-bottom transport of cool waters toward this island. Because the slope S is directed in the radial direction r, near-bottom movements in the r direction are directly proportional to the vertical motions. Upon integrating the radial direction transport term in the r and z directions, the radial spatial gradient drops out (i.e., $\iint \frac{\partial}{\partial r}\overline{u_r T'} dr dz = \int \overline{u_r T'} dz$). Therefore, we define upwelling as the cross-slope heat transport near the bottom of the water column,

$$\int_{-H}^{\zeta_0} \overline{u_r T'} dz = \int_{-H}^{\zeta_0} \overline{u_r}\,\overline{T'} dz + \int_{-H}^{\zeta_0} \overline{\tilde{u}_r \tilde{T}'} dz \tag{20}$$

where the two terms on the right represent the transport of heat from mean currents and the transport of heat from waves respectively. ζ_0 represents a constant density, here chosen as the density corresponding to 2/3 of the depth at the initial condition. Assuming transport across ζ_0 is negligible, this formulation is Lagrangian and should capture the heat transport from features such as trapped cores. The limits of depth integration from $-H$ to ζ_0 were chosen to capture the near bottom effects while being large enough to cover several z-levels.

The net upwelling is positive along the eastern side of the island leading to cooling of the near-bottom waters (Figures 4i and 4j), and this effect is due almost entirely due the wave transport term in Equation 20 (i.e., $\int_{-H}^{\zeta_0} \overline{u_r}\,\overline{T'} dz \approx 0$). For the no rotation case R2, the results are quite similar (Figure S2 in Supporting Information S1).

The average temperature disturbance from the background (offshore) state $\overline{T'}$ is a measure of the upwelling effects of the mean flows. Results for the base case R1 show cooler and denser upwelled water near the surface, and cooler dense water on the east side of the island compared to the west (Figure 11a). Density differences are larger in case R2 compared to case R1 in the shallow slope region (Figure 11b). The higher FR case (R3) higher Ex case (R6) and barotropic mean flow case (R7) density patterns are similar to case R1 (Figures 11c, 11f, and 11g). The subcritical slope case (R4) temperature is significantly more variable than case R1 with more dense upwelled water on the east of the island, and less dense water present on the west side (Figure 11d). The barotropic tide case (R5) is significantly more variable than case R1 near the surface, while differences deeper in the water column are similar (Figure 11e). In summary, all simulations show cooler and denser upwelled water in the shallow slope region as a result of wave-driven upwelling.

3.3.2. Upwelling Effects

The upwelling of deep ocean waters to shallow regions can occur from several processes such as transport from the internal waves directly (Arthur et al., 2017; Arthur & Fringer, 2016; Davis et al., 2020) from tilting of the isopycnal lines due to large scale flows (R7), or oscillation of the isopycnal lines due to barotropic tides (R6). As demonstrated in Section 3.3, upwelling in this context is primarily driven by the near-bottom transport of

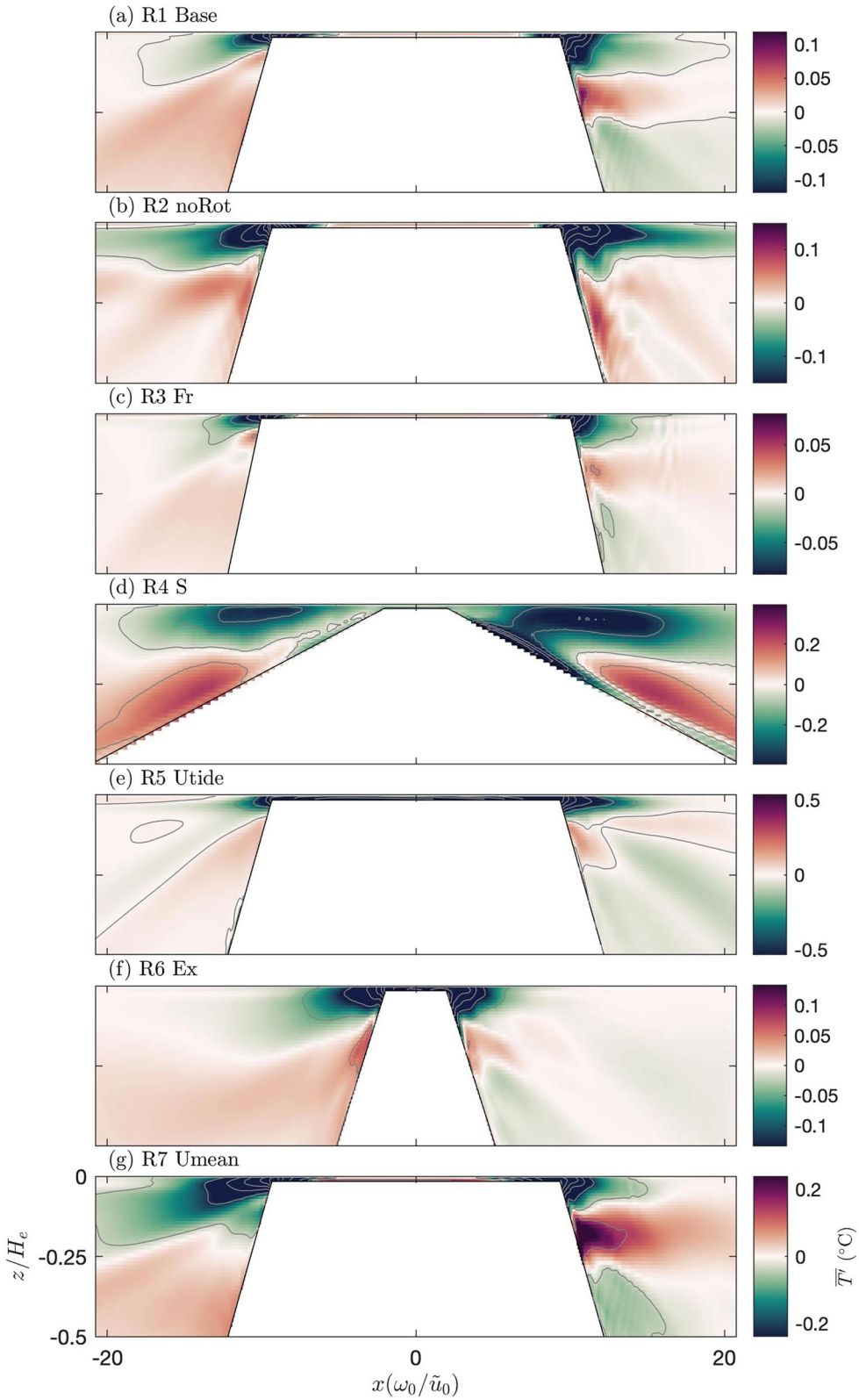

Figure 11. Average temperature disturbance from background $\overline{T'}$ for different simulations R1–R7 from side view (x, z), where internal tides are propagating from right to left in this view, gray lines are contours of average temperature. Note the color scales vary in each panel, and horizontal scales are normalized by $\tilde{u}_0/\omega_0$, where the absolute scale of island is given by W in Table 1.

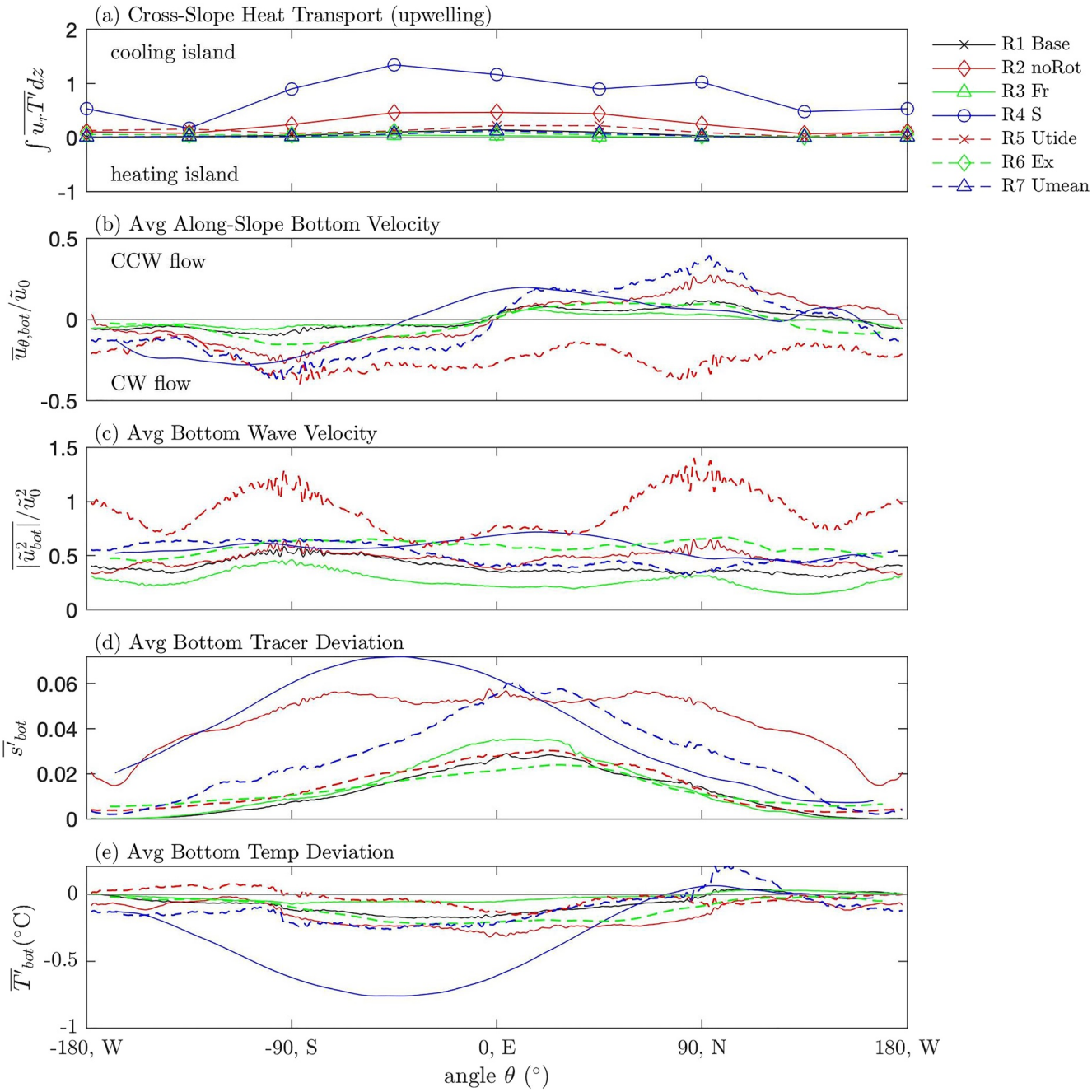

Figure 12. Representative heat transport and ecologically important parameters in shallow depths in the circumference around the island showing (a) cross-slope heat transport where + sign is an island cooling effect, (b) near-bottom average along-slope velocity $\overline{u}_{\theta,\mathrm{bot}}/\tilde{u}_0$ (c) near-bottom average wave velocity $\overline{|\tilde{u}^2_{\mathrm{bot}}|}/\tilde{u}^2_0$, (d) near-bottom average passive tracer deviation from offshore $\overline{s'}_{\mathrm{bot}}$, and (e) near-bottom average temperature deviation from offshore $\overline{T'}_{\mathrm{bot}}$. For (a), integral in z is taken over the bottom of the water column ($\int_{-H}^{\zeta_0} dz$), and radial position is at $H/H_e = 0.52$. For (b–e) the near bottom quantities are averaged over shallow areas between 8 and 60 m depth ($H/H_e = 0.19$) within shallow and upper mesophotic depth zones, as a function of along-slope position.

cooler dense waters upslope by waves (Figures 4i and 4j) and all simulations show denser upwelled water in the shallow slope region based on the average density variation from background (Figure 11). Upwelling is strongest along the eastern side of the island, and when compared across the simulations, upwelling is strongest in the subcritical slope case (R4), and the no rotation case (R2) (Figure 12a). The effect of this upwelling for the no rotation case R2 and subcritical slope case R4 is shown by increased near bottom tracer $\overline{s'}_{\mathrm{bot}}$ (Figure 12d) which originated below 100 m depth (Figure 2c). In addition, the results show decreased near-bottom temperature $\overline{T'}_{\mathrm{bot}}$

(Figure 12e) in the shallow depths around the island. The subcritical slope case R4 shows significant asymmetry in the upwelling, which is most likely related to the enhanced wave motions for subcritical slope acting in concert with rotational effects. The barotropic tide case R5 does not show significant changes to the shallow temperature or tracers compared to R1, but in regions with complex geometries such as inlets, steep slopes or headlands, locally generated bores from barotropic tide forcing can be significant (Green et al., 2019). The mean flow case R7 also shows some increased near-bottom tracer along the eastern side of the island (Figure 12d), which is likely the result of mean flows interacting with the internal tides (which are coaligned in this case) to enhance upwelling of tracers. These results are consistent with field observations of upwelling and bifurcation of flows at depth from mean flows (Jakoboski et al., 2020).

In summary, shoaling internal waves transport deeper waters into the very shallow regions for all modeled conditions, but were enhanced for subcritical slopes and low Rossby numbers. Globally, we would expect these conditions where subcritical slopes exist, or even where portions of the slope are subcritical. We would also expect enhanced upwelling in lower latitudes.

3.4. Ecologically Relevant Effects

An important aspect of these results is their relevance to the ecology of benthic organisms. In general, internal wave motions increase near bed flows and are typically considered favorable to benthic organisms as long as the currents are not so large that they result in damage (Bilger & Atkinson, 1992; Carpenter et al., 1991; Genin et al., 2009). Deeper upwelled waters are also generally considered a favorable source of nutrients for benthic organisms, although prolonged exposure to deep waters such as low oxygen can be harmful (Williams et al., 2018) and there are cases where the upwelling of deep waters with very strong temperature gradients have been considered stressful and higher nutrient concentrations favoring the growth of macroalgae and not coral (Johannes et al., 1983; Lapointe, 1997). In the face of climate change, it is of special interest to understand locations which will create favorable conditions for these benthic organisms, and especially reduced bottom temperatures compared to surrounding waters which would alleviate thermal stress and create thermal refuges (Reid et al., 2019; Storlazzi et al., 2020; Wyatt et al., 2020). Thus, while exceptions can be made, generally higher wave motions (from surface or internal waves), upwelled deep waters in the shallow regions and lower temperatures may considered favorable for benthic organisms.

From the cases presented in this work, we compare the average wave velocity variance normalized by the offshore internal wave motions $\overline{|\tilde{u}^2_{bot}|}/\tilde{u}^2_0$ (Figure 12c) (surface waves are not considered here), the deviation of the near-bottom average tracer from the offshore concentration $\overline{s'}_{bot}$ (Figure 12d), and the deviation of near-bottom average temperature from the offshore temperature $\overline{T'}_{bot}$ (Figure 12e). We then spatially average these values over the shallow upper mesophotic depth zone (<60 m) as a function of the position around the island.

The average wave velocities are similar for most of the model simulations with little variation around the island. The exception is the barotropic tide case (R5) which has enhanced internal wave velocities by a factor of two compared to case R1 along the north and south sides of the island where flow is impinging on the island from the east-west tide oscillations. It is unclear if local internal tides are generated by the barotropic tide in R5, but this is a promising avenue for future work.

The average tracer concentrations are highest along the eastern side of the island for all simulations consistent with the direction of incoming internal waves. Both the no rotation (R2) and subcritical slope (R4) have more upwelled deep waters in the shallow regions compared to case R1 all around the island, discussed in detail in Section 4.3. The barotropic mean flow case (R7) also shows enhanced tracer concentrations, centered along the east side of the island.

The average temperature is similar for most of the model simulations with approximately 0.2°C lower average temperature compared to the offshore along the east side of the island. The exception is the subcritical slope simulation (R4) which shows 0.7°C of average cooling along the south to east sides of the island. Thus, of the conditions evaluated, most runs show only a slight cooling effect from the internal tides, but the subcritical slope case shows significant potential for cooling. The present study does not have atmospheric forcing or an interior lagoon system which can be present on islands and alter the shallow near-island temperatures significantly

(Davis et al., 2020; Reid et al., 2019). The interplay between upwelled waters from internal tides and shallow atmospheric effects would be an avenue for future study.

All simulations showed upwelled deep waters in the shallow regions, and some limited cooling effects on the eastern side of the island consistent with the direction of the incoming internal tides. The barotropic tides can move water efficiently, but without upwelled deep waters in the shallow regions or cooler waters, it is uncertain how beneficial that would be to benthic organisms. The cases without rotation and high barotropic mean flows create mixing and upwelled tracers in the shallow regions but have minimal effect on cooling. However, the subcritical slope case has moderately high internal wave motions, upwelled deep waters in the shallow regions and significantly cooler temperature. Thus, of all the cases, the subcritical slope case may have the greatest potential for creating favorable conditions for benthic organisms. Globally, the magnitude of cooling and concentrations of tracers would change depending on the stratification. Therefore, we may expect ecologically favorable conditions in areas with strong stratification, strong internal tides, and subcritical slopes. These regions may buffer benthic communities and provide thermal refugia from future ocean warming.

4. Summary

We present a modeling study of an idealized island with sloping sides in a stratified ocean with internal tides propagating through the domain, which transform into nonlinear internal waves as they encounter shallow depths. In the base case R1 which is representative of a mid-latitude island with relatively steep super critical slopes, the nonlinear internal waves shoaling on the island wrap around the island, scatter, and create an asymmetric wavefield. The nonlinear internal waves create residual currents and upwelling of deeper ocean tracers. We explore the effects of different physical parameters including no rotation (R2), higher Froude number (R3), subcritical slope (R4), addition of barotropic tides (R5), larger excursion number (R6), and addition of large scale mean currents (R7). The subcritical slope has the greatest potential for creating enhanced upwelling. Areas of the world's oceans with stratified waters sufficient to sustain internal tide motions, strong internal tide energy, and local subcritical bottom slopes are likely to have cooler waters and more upwelled deep waters than the surrounding areas.

Data Availability Statement

SUNTANS model run output is publicly available at https://purl.stanford.edu/td688wq5586 and model code is available at https://github.com/rogersjs77/suntans/tree/nesting_iwaves.

Acknowledgments
This research is supported by ONR Grants N00014-15-1-2287, N00014-16-1-2256, and N00014-20-1-2707. K. Davis was further supported by NSF Grant OCE-1753317 and ONR Grant N00014-22-1-2040. The authors thank Stephen Monismith, Geno Pawlak, and Leif Thomas for helpful discussions and reviews from two anonymous reviewers which improved the quality of the manuscript. The authors gratefully acknowledge the US Army Research Laboratory DoD Supercomputing Resource Center for computer time on Excalibur and Onyx.

References

Alford, M. H., Peacock, T., MacKinnon, J. A., Nash, J. D., Buijsman, M. C., Centuroni, L. R., et al. (2015). The formation and fate of internal waves in the South China Sea. *Nature*, *521*(7550), 65–69. https://doi.org/10.1038/nature14399

Arthur, R. S., & Fringer, O. B. (2016). Transport by breaking internal gravity waves on slopes. *Journal of Fluid Mechanics*, *789*(2014), 93–126. https://doi.org/10.1017/jfm.2015.723

Arthur, R. S., Koseff, J. R., & Fringer, O. B. (2017). Local versus volume-integrated turbulence and mixing in breaking internal waves on slopes. *Journal of Fluid Mechanics*, *815*, 169–198. https://doi.org/10.1017/jfm.2017.36

Bai, X., Li, X., Lamb, K. G., & Hu, J. (2017). Internal solitary wave reflection near Dongsha atoll, the south China Sea. *Journal of Geophysical Research: Oceans*, *122*(10), 7978–7991. https://doi.org/10.1002/2017JC012880

Bilger, R. W., & Atkinson, M. J. (1992). Anomalous mass transfer of phosphate on coral reef flats. *Limnology & Oceanography*, *37*(2), 261–272. https://doi.org/10.4319/lo.1992.37.2.0261

Boegman, L., Ivey, G. N., & Imberger, J. (2005). The degeneration of internal waves in lakes with sloping topography. *Limnology & Oceanography*, *50*(5), 1620–1637. https://doi.org/10.4319/lo.2005.50.5.1620

Carpenter, R. C., Hackney, J. M., & Adey, W. H. (1991). Measurements of primary productivity and nitrogenase activity of coral reef algae in a chamber incorporating oscillatory flow. *Limnology & Oceanography*, *36*(1), 40–49. https://doi.org/10.4319/lo.1991.36.1.0040

Casulli, V., & Zanolli, P. (2005). High resolution methods for multidimensional advection-diffusion problems in free-surface hydrodynamics. *Ocean Modelling*, *10*(1–2), 137–151. https://doi.org/10.1016/j.ocemod.2004.06.007

Chao, S. Y., Shaw, P. T., Hsu, M. K., & Yang, Y. J. (2006). Reflection and diffraction of internal solitary waves by a circular island. *Journal of Oceanography*, *62*(6), 811–823. https://doi.org/10.1007/s10872-006-0100-4

Davis, K. A., Arthur, R. S., Reid, E. C., Rogers, J. S., Fringer, O. B., DeCarlo, T. M., & Cohen, A. L. (2020). Fate of internal waves on a shallow shelf. *Journal of Geophysical Research: Oceans*, *125*, 1–18. https://doi.org/10.1029/2019jc015377

Eriksen, C. C. (1982). Observations of internal wave reflection off sloping bottoms. *Journal of Geophysical Research*, *87*(C1), 525–538. https://doi.org/10.1029/JC087iC01p00525

Farmer, D., Li, Q., & Park, J. (2009). Internal wave observations in the South China Sea: The role of rotation and non-linearity. *Atmosphere-Ocean*, *47*(4), 267–280. https://doi.org/10.3137/OC313.2009

Fringer, O. B., Gerritsen, M., & Street, R. L. (2006). An unstructured-grid, finite-volume, nonhydrostatic, parallel coastal ocean simulator. *Ocean Modelling*, *14*(3–4), 139–173. https://doi.org/10.1016/j.ocemod.2006.03.006

Fringer, O. B., & Street, R. L. (2003). The dynamics of breaking progressive interfacial waves. *Journal of Fluid Mechanics*, *494*, 319–353. https://doi.org/10.1017/S0022112003006189

Genin, A., Monismith, S. G., Reidenbach, M. A., Yahel, G., & Koseff, J. R. (2009). Intense benthic grazing of phytoplankton in a coral reef. *Limnology & Oceanography*, *54*(3), 938–951. https://doi.org/10.4319/lo.2009.54.3.0938

Gove, J. M., McManus, M. A., Neuheimer, A. B., Polovina, J. J., Drazen, J. C., Smith, C. R., et al. (2016). Near-island biological hotspots in barren ocean basins. *Nature Communications*, *7*, 1–34. https://doi.org/10.1038/ncomms10581

Green, R. H., Jones, N. L., Rayson, M. D., Lowe, R. J., Bluteau, C. E., & Ivey, G. N. (2019). Nutrient fluxes into an isolated coral reef atoll by tidally driven internal bores. *Limnology & Oceanography*, *64*(2), 461–473. https://doi.org/10.1002/lno.11051

Hall, R. A., Huthnance, J. M., & Williams, R. G. (2013). Internal wave reflection on shelf slopes with depth-varying stratification. *Journal of Physical Oceanography*, *43*(2), 248–258. https://doi.org/10.1175/JPO-D-11-0192.1

Helfrich, K. R. (2007). Decay and return of internal solitary waves with rotation. *Physics of Fluids*, *19*(2). https://doi.org/10.1063/1.2472509

Hogg, N. G. (1971). Longshore current generation by obliquely incident internal waves. *Geophysical Fluid Dynamics*, *2*(1), 361–376. https://doi.org/10.1080/03091927108236070

Jakoboski, J., Todd, R. E., Brechner Owens, W., Karnauskas, K. B., & Rudnick, D. L. (2020). Bifurcation and upwelling of the equatorial undercurrent west of the galápagos archipelago. *Journal of Physical Oceanography*, *50*(4), 887–905. https://doi.org/10.1175/JPO-D-19-0110.1

Jalali, M., Rapaka, N. R., & Sarkar, S. (2014). Tidal flow over topography: Effect of excursion number on wave energetics and turbulence. *Journal of Fluid Mechanics*, *750*(3), 259–283. https://doi.org/10.1017/jfm.2014.258

Johannes, R., Wiebe, W., Crossland, C., Rimmer, D., & Smith, S. (1983). Latitudinal limits of coral reef growth. *Marine Ecology Progress Series*, *11*, 105–111. https://doi.org/10.3354/meps011105

Kang, D., & Fringer, O. (2012). Energetics of barotropic and baroclinic tides in the Monterey Bay area. *Journal of Physical Oceanography*, *42*(2), 272–290. https://doi.org/10.1175/JPO-D-11-039.1

Kundu, P. K., & Cohen, I. M. (2008). *Fluid mechanics* (4th ed.). Academic Press.

Lamb, K. G. (2013). Internal wave breaking and dissipation mechanisms on the continental slope/shelf. *Annual Review of Fluid Mechanics*, *46*(1), 231–254. https://doi.org/10.1146/annurev-fluid-011212-140701

Lamb, K. G. (2014). Internal wave breaking and dissipation mechanisms on the continental slope/shelf. *Annual Review of Fluid Mechanics*, *46*(1), 231–254. https://doi.org/10.1146/annurev-fluid-011212-140701

Lapointe, B. E. (1997). Nutrient thresholds for bottom-up control of macroalgal blooms on coral reefs in Jamaica and southeast Florida. *Limnology & Oceanography*, *42*(5 II), 1119–1131. https://doi.org/10.4319/lo.1997.42.5_part_2.1119

Lien, R.-C., Henyey, F., Ma, B., & Yang, Y. J. (2014). Large-amplitude internal solitary waves observed in the northern south China Sea: Properties and energetics. *Journal of Physical Oceanography*, *44*(4), 1095–1115. https://doi.org/10.1175/JPO-D-13-088.1

Liu, Z., Wu, L., & Bayler, E. (1999). Rossby wave-coastal Kelvin wave interaction in the extratropics. Part I: Low-frequency adjustment in a closed basin. *Journal of Physical Oceanography*, *29*(9), 2382–2404. https://doi.org/10.1175/1520-0485(1999)029<2382:RWCKWI>2.0.CO;2

Loder, J. W. (1980). Topographic rectification of tidal currents on the sides of Georges Bank. *Journal of Physical Oceanography*(9), 1399–1416. https://doi.org/10.1175/1520-0485(1980)010<1399:trotco>2.0

Masunaga, E., Arthur, R. S., & Fringer, O. B. (2019). Internal wave breaking dynamics and associated mixing in the coastal ocean. *Encyclopedia of ocean sciences* (3rd ed.). Elsevier Ltd. https://doi.org/10.1016/B978-0-12-409548-9.10953-4

Masunaga, E., Fringer, O. B., Kitade, Y., Yamazaki, H., & Gallager, S. M. (2017). Dynamics and energetics of trapped diurnal internal Kelvin waves around a midlatitude island. *Journal of Physical Oceanography*, *47*(10), 2479–2498. https://doi.org/10.1175/jpo-d-16-0167.1

McSweeney, J. M., Lerczak, J. A., Barth, J. A., Becherer, J., Colosi, J. A., Mackinnon, J. A., et al. (2019). Observations of shoaling nonlinear internal bores across the Central California inner shelf. *Journal of Physical Oceanography*, *49*(10), 111–132. https://doi.org/10.1175/JPO-D-19-0125.1

Nash, J. D., Kunze, E., Toole, J. M., & Schmitt, R. W. (2004). Internal tide reflection and turbulent mixing on the continental slope. *Journal of Physical Oceanography*, *34*(5), 1117–1134. https://doi.org/10.1175/1520-0485(2004)034<1117:ITRATM>2.0.CO;2

Ramp, S. R., Yang, Y. J., & Bahr, F. L. (2010). Characterizing the nonlinear internal wave climate in the northeastern South China Sea. *Nonlinear Processes in Geophysics*, *17*(5), 481–498. https://doi.org/10.5194/npg-17-481-2010

Reid, E. C., DeCarlo, T. M., Cohen, A. L., Wong, G. T. F., Lentz, S. J., Safaie, A., et al. (2019). Internal waves influence the thermal and nutrient environment on a shallow coral reef. *Limnology & Oceanography*(5), 1–17. https://doi.org/10.1002/lno.11162

Rogers, J. S., Rayson, M. D., Ko, D. S., Winters, K. B., & Fringer, O. B. (2019). A framework for seamless one-way nesting of internal wave-resolving ocean models. *Ocean Modelling*, *143*(March), 101462. https://doi.org/10.1016/j.ocemod.2019.101462

Scotti, A., Beardsley, R. C., & Butman, B. (2007). Generation and propagation of nonlinear internal waves in Massachusetts Bay. *Journal of Geophysical Research*, *112*(10), 1–19. https://doi.org/10.1029/2007JC004313

Signell, R. P., & Geyer, W. R. (1991). Transient eddy formation around headlands. *Journal of Geophysical Research*, *96*(C2), 2561–2575. https://doi.org/10.1029/90jc02029

Storlazzi, C. D., Cheriton, O. M., van Hooidonk, R., Zhao, Z., & Brainard, R. (2020). Internal tides can provide thermal refugia that will buffer some coral reefs from future global warming. *Scientific Reports*, *10*(1), 1–9. https://doi.org/10.1038/s41598-020-70372-9

Suanda, S. H., Feddersen, F., & Kumar, N. (2017). The effect of barotropic and baroclinic tides on coastal stratification and mixing. *Journal of Geophysical Research: Oceans*, *122*(12), 10156–10173. https://doi.org/10.1002/2017JC013379

Thomson, R. E., & Wilson, R. E. (1987). Coastal countercurrent and mesoscale eddy formation by tidal rectification near an oceanic cape. *Journal of Physical Oceanography*(11), 2096–2126. https://doi.org/10.1175/1520-0485(1987)017<2096:ccamef>2.0.co;2

Thorpe, S. A. (1999). The generation of alongslope currents by breaking internal waves. *Journal of Physical Oceanography*, *29*(1), 29–38. https://doi.org/10.1175/1520-0485(1999)029<0029:TGOACB>2.0.CO;2

Vitousek, S., & Fringer, O. B. (2011). Physical vs. numerical dispersion in nonhydrostatic ocean modeling. *Ocean Modelling*, *40*(1), 72–86. https://doi.org/10.1016/j.ocemod.2011.07.002

Vitousek, S., & Fringer, O. B. (2014). A nonhydrostatic, isopycnal-coordinate ocean model for internal waves. *Ocean Modelling*, 118–144. https://doi.org/10.1016/j.ocemod.2014.08.008

Walter, R. K., Woodson, C. B., Arthur, R. S., Fringer, O. B., & Monismith, S. G. (2012). Nearshore internal bores and turbulent mixing in southern Monterey Bay. *Journal of Geophysical Research*, *117*(C7), C07017. https://doi.org/10.1029/2012JC008115

Wang, Y. H., Dai, C. F., & Chen, Y. Y. (2007). Physical and ecological processes of internal waves on an isolated reef ecosystem in the South China Sea. *Geophysical Research Letters*, *34*(18), 1–7. https://doi.org/10.1029/2007GL030658

Williams, G. J., Sandin, S. A., Zgliczynski, B. J., Fox, M. D., Gove, J. M., Rogers, J. S., et al. (2018). Biophysical drivers of coral trophic depth zonation. *Marine Biology*, *165*(4), 60. https://doi.org/10.1007/s00227-018-3314-2

Winters, K. B. (2015). Tidally-forced flow in a rotating, stratified, shoaling basin. *Ocean Modelling*, *90*, 72–81. https://doi.org/10.1016/j.ocemod.2015.04.004

Wunsch, C. (1968). On the propagation of internal waves up a slope. *Deep-Sea Research and Oceanographic Abstracts*, *15*(3), 258. https://doi.org/10.1016/0011-7471(68)90002-8

Wyatt, A. S. J., Leichter, J. J., Toth, L. T., Miyajima, T., Aronson, R. B., & Nagata, T. (2020). Heat accumulation on coral reefs mitigated by internal waves. *Nature Geoscience*, *13*(1), 28–34. https://doi.org/10.1038/s41561-019-0486-4

Zhang, Z., Fringer, O. B., & Ramp, S. R. (2011). Three-dimensional, nonhydrostatic numerical simulation of nonlinear internal wave generation and propagation in the South China Sea. *Journal of Geophysical Research*, *116*(5), 1–26. https://doi.org/10.1029/2010JC006424